www.acsnano.org

# Cell-Membrane Coated Nanoparticles for Tumor Delineation and Qualitative Estimation of Cancer Biomarkers at Single Wavelength Excitation in Murine and Phantom Models

Indrajit Srivastava,\* Benjamin Lew, Yuhan Wang, Steven Blair, Mebin Babu George, Brianna Scheid Hajek, Sushant Bangru, Subhendu Pandit, Ziwen Wang, Jamie Ludwig, Kristen Flatt, Martin Gruebele, Shuming Nie,\* and Viktor Gruev\*



Downloaded via UNIV ILLINOIS URBANA-CHAMPAIGN on May 9, 2023 at 15:58:53 (UTC). See https://pubs.acs.org/sharingguidelines for options on how to legitimately share published articles.

Cite This: ACS Nano 2023, 17, 8465-8482



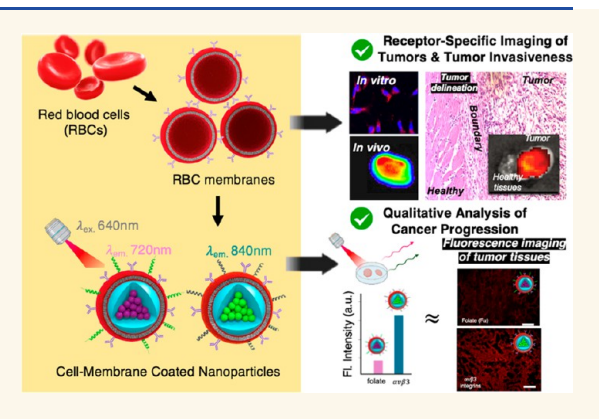
**ACCESS** 

III Metrics & More

Article Recommendations

Supporting Information

ABSTRACT: Real-time guidance through fluorescence imaging improves the surgical outcomes of tumor resections, reducing the chances of leaving positive margins behind. As tumors are heterogeneous, it is imperative to interrogate multiple overexpressed cancer biomarkers with high sensitivity and specificity to improve surgical outcomes. However, for accurate tumor delineation and ratiometric detection of tumor biomarkers, current methods require multiple excitation wavelengths to image multiple biomarkers, which is impractical in a clinical setting. Here, we have developed a biomimetic platform comprising near-infrared fluorescent semiconducting polymer nanoparticles (SPNs) with red blood cell membrane (RBC) coating, capable of targeting two representative cell-surface biomarkers (folate,  $\alpha v \beta 3$  integrins) using a single excitation wavelength for tumor delineation during surgical interventions. We evaluate our single excitation ratiometric nano-



particles in *in vitro* tumor cells, *ex vivo* tumor-mimicking phantoms, and *in vivo* mouse xenograft tumor models. Favorable biological properties (improved biocompatibility, prolonged blood circulation, reduced liver uptake) are complemented by superior spectral features: (i) specific fluorescence enhancement in tumor regions with high tumor-to-normal tissue (T/NT) ratios in *ex vivo* samples and (ii) estimation of cell-surface tumor biomarkers with single wavelength excitation providing insights about cancer progression (metastases). Our single excitation, dual output approach has the potential to differentiate between the tumor and healthy regions and simultaneously provide a qualitative indicator of cancer progression, thereby guiding surgeons in the operating room with the resection process.

**KEYWORDS:** red-blood-cell membranes, semiconducting polymer nanoparticles, near-infrared fluorescence, tumor delineation, biomarker expression, single wavelength excitation

# **INTRODUCTION**

Surgical resection is often the most effective treatment option for many solid tumors including stage I–III breast cancer, <sup>1–3</sup> despite the availability of chemotherapy and radiotherapy. <sup>4</sup> In resection, the complete removal of primary tumors to achieve negative surgical margins (as referred by surgeons) is of paramount importance to minimize tumor recurrence. <sup>5,6</sup> Unfortunately, tumor margins are often indistinct and irregular due to the invasive nature of the primary tumors on the surrounding healthy tissues. Hence, in many cases, surgeons will need to routinely resect large margins of healthy tissues to avoid leaving any tumor lesions behind. This approach often leads to

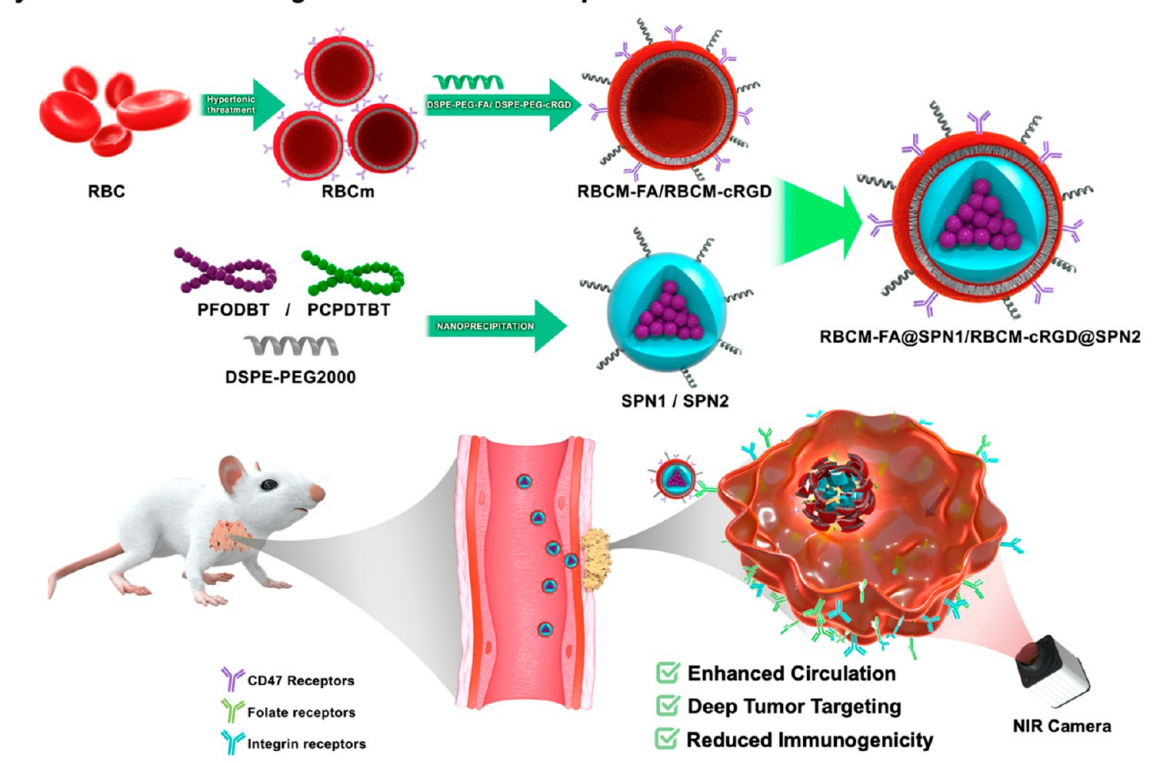
the unnecessary removal of healthy tissues in important locations such as blood vessels and nerves, causing neurological damage, increasing mortality, and ultimately reducing the patient's quality of life.<sup>7,8</sup> One of the methods used by surgeons

Received: January 19, 2023 Accepted: April 19, 2023 Published: April 26, 2023

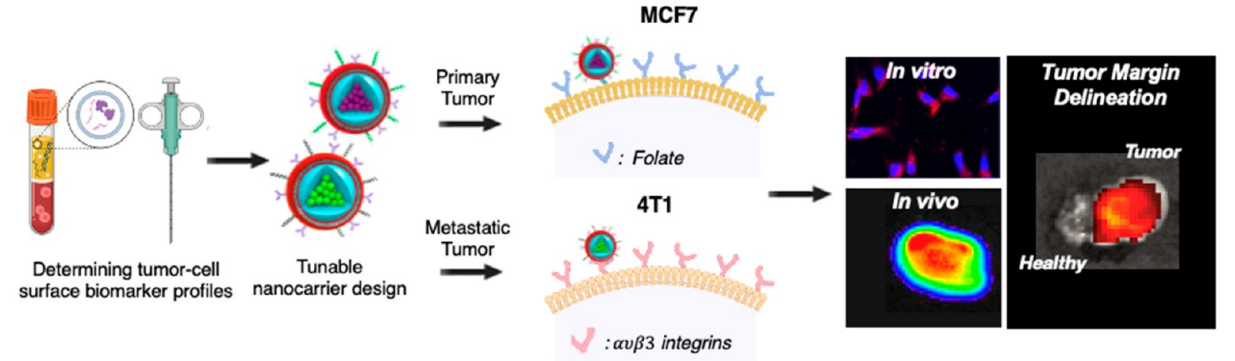




# **a** Synthesis of Tumor-Targeted Biomimetic Nanoparticles



# **b** Receptor-Specific Imaging of Tumor & Tumor Margin Delineation



# C Qualitative Estimation of Tumor Biomarkers at Single Wavelength Excitation

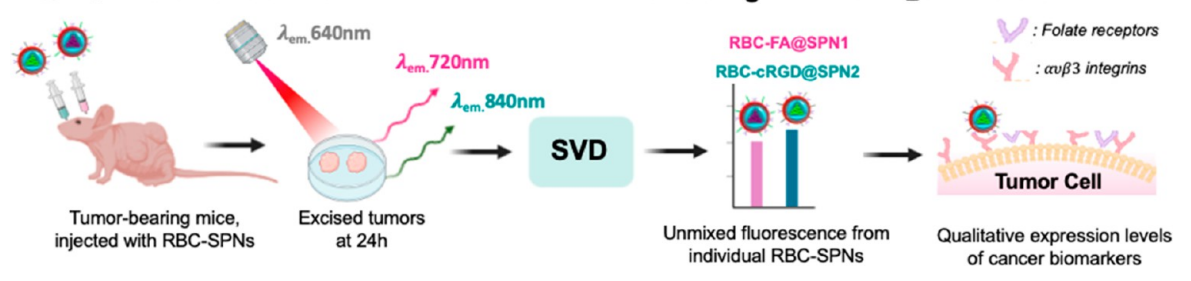


Figure 1. (a) Schematic representation showing extraction of RBCm, imparting it with tumor-targeting peptides, and consequently encapsulating with SPs to form biomimetic semiconducting polymers, RBC-SPNs. These RBC-SPNs have properties including enhanced circulation in the blood, precise tumor targeting, and enhanced biocompatibility. (b) Depending on the peptide—lipid inserted, different cell-surface tumor biomarkers could be targeted *in vitro* and *in vivo*. They can be further used for tumor delineation, distinctly highlighting the tumor regions. (c) Schematic workflow for multiplexed optical imaging at single wavelength excitation in tumor-mimicking phantoms using singular value decomposition to determine the concentration of two RBC-SPNs, eventually correlating to qualitative expression levels of cancer biomarkers.

to detect the tumor margins in an intraoperative setting relies on the hands (palpation) and eyes (visual inspection) to differentiate cancer tissues from healthy tissues. However, relying on such information to make a surgical cut has often proven to be risky because many cancers are not palpable and lead to high positive margin rates during the surgery.  $^{9-11}$ 

Fluorescence-based image-guided surgery (FIGS) has shown great promise to provide surgeons with real-time feedback on tumors in an intraoperative setting. 12-14 FIGS offers numerous advantages over conventional imaging modalities by providing high spatial resolution and the absence of ionizing radiation. FIGS is usually reliant on the near-infrared (NIR) range (700– 900 nm) that is superior to the visible spectrum owing to low tissue autofluorescence, low scattering, and comparatively higher tissue penetration. Hence, FIGS systems need a NIR fluorescent imaging agent that could selectively accumulate in the tumors, assisting with the surgical intervention procedure. Currently, there are a few FDA-approved fluorophores utilized for FIGS, while there is a multitude of targeted fluorescent probes in the clinical and preclinical developmental stages. 15-17 One such approved probe is indocyanine green (ICG), which is optically active in the NIR range and has been chemically modified to target tumors for investigative human trials involving solid tumors or sentinel lymph nodes. 18–20

With the advent of nanotechnology, different nanoparticlebased contrast agents have been developed for FIGS applications including semiconductor quantum dots, carbon dots, metallic nanoparticles, and organic nanoparticles.<sup>21-25</sup> Recently, semiconducting polymeric nanoparticles (SPNs) have emerged as a promising class of imaging nanoagents composed of optically active semiconducting polymers (SPs) that are completely organic and biologically inert. These nanoagents could essentially lower issues posed by heavy metal ion-induced toxicity to living organisms. 20,26-28 Owing to their high absorption coefficients and tunable dimensions, SPNs have been utilized for a multitude of applications such as cell tracking, tumor imaging, brain imaging, and drug-induced hepatotoxicity evaluation. 29-32 Nevertheless, all these nanoparticle-based contrast agents suffer from at least one issue that has been limiting their potential clinical applications including (i) rapid clearance from the blood and subsequent filtration by the renal and reticuloendothelial system (RES), (ii) increased nonspecific binding from proteins impeding the tumor-targeting capability, (iii) variable brightness of the probe in an in vivo scenario resulting in low tumor to normal tissue ratio, and (iv) limited time frame in which the imaging needs to be done due to eventual fluorescence quenching of the probe. Cell membrane coating nanotechnology has emerged as a biomimetic strategy that has the potential to overcome these limitations. It has been successfully used for drug delivery, cancer therapeutic, and theranostic applications. The cell membrane contains adhesion proteins, antigens, and membrane structures that can be successfully coated onto nanoparticles and imparts them with the functions of the natural cell membranes. For example, the intrinsic ability of red blood cells to evade the immune system and prolonged blood circulation has been utilized by coating red blood cell membranes onto nanoparticles for theranostic applications.<sup>37-39</sup> Such strategies could be important for fluorescence-guided surgical applications where reduced uptake by liver macrophages would indirectly correlate to higher uptake of nanoparticles into tumors, resulting in high tumor-tobackground signals. However, to the best of our knowledge, there are no studies that explore the potential of such biomimetic nanoparticles for fluorescence-guided surgical applications.

In this study, we have developed NIR imaging agents comprising SPNs as the core and tumor-targeted biomimetic red-blood-cell membranes (RBCm) as the shell. The SPNs are responsive to generating NIR optical signal and the surface

coating of targeted RBCm imparts them with favorable biological properties of increased biocompatibility, prolonged in vivo blood circulation, and reduced liver uptake (Figure 1a). With a facile lipid-insertion strategy previously optimized by us and others, the ability to target two representative cell-surface biomarkers (folate,  $\alpha v \beta 3$  integrins) was imparted to RBC-SPNs. These receptor-specific biomimetic nanoparticles showed significantly high tumor-to-normal tissue ratios, precisely delineating tumor regions from healthy regions (Figure 1b). Finally, at single excitation and having spectrally distinct emission, these dual biomimetic nanoparticles were used for qualitative estimation of cancer biomarkers at single-wavelength-excitation (Figure 1c). Having fluorescence contributions from nanoparticles targeting two representative tumor-cell surface biomarkers will be able to account for the tumor heterogeneity issues that are often associated with solid tumors and provide vital information about cancer progression (i.e., metastases). For accurate tumor delineation and ratiometric detection of tumor biomarkers, current methods require multiple excitation wavelengths to image multiple biomarkers, which is impractical in a clinical setting. The ability of two nanoparticles to be excited at single-wavelength-excitation will further benefit incorporating imaging sensors in an operating suite. First, the optical setup will be simplified, and overall cost is reduced when a single excitation wavelength is utilized. Only one laser and necessary optics on the camera side to remove excitation light source are required. Second, the acquisition of imaging spectrum is increased when a single excitation wavelength is used. Since only one notch filter is used to remove the single excitation light source, the imaging spectrum for both SPNs is improved, which can lead to better discrimination and higher signal-to-noise ratio imaging. The two representative cancer biomarkers selected in this study were folate receptors and  $\alpha v \beta 3$  integrins. Folate receptors are overexpressed in many human cancers, especially primary tumors.  $\alpha v \beta 3$  integrins have been associated with angiogenesis and metastasis, thus prevalent in metastatic tumors. We validated these features using in vitro cells, in vivo and ex vivo preclinical tumor-bearing mice models, and ex vivo tumormimicking phantoms. As shown by our follow-up assessments using statistical tools, RNA sequencing, and histopathology results, biomimetic nanoparticles provide both qualitative and semiquantitative information about cancer progression.

Collectively, our single excitation, dual output approach has the potential to differentiate between the tumor and healthy regions and simultaneously provide a qualitative indicator of cancer progression, thereby guiding surgeons in the operating room with the resection process.

# **RESULTS AND DISCUSSION**

Rational Selection of SPs, Synthesis of SPNs, and their Physicochemical and Optical Characterization. The semiconducting polymers (SPs) can be bandgap-engineered to have a small HOMO–LUMO energy gap to yield NIR fluorescence emission. For attaining NIR emission, electronrich donor and electron-poor acceptor chemical moieties are alternatingly arranged to form a conjugated polymer with highlying HOMO (centered on the donor) and low-lying LUMO (centered on the acceptor). Such donor—acceptor arrangements are usually synthesized by metal-catalyzed cross-coupling reactions such as Suzuki coupling. For our study, we selected two SPs already known in the literature to make SPNs that have been shown to demonstrate NIR emission: PFODBT (SP1)<sup>31</sup>

having an emission maximum of 720 nm, and PCPDTBT (SP2)<sup>41</sup> having an emission maximum of 840 nm. The rationale behind this choice was 2-fold: (i) the two NIR-emitting SPNs can target two distinct cancer biomarkers on tumor metastases, and (ii) the SPNs can be excited at a single-laser wavelength, simplifying the optical imaging setup. The latter could be vital for studies involving imaging multiple-tumor cell surfaces at single-laser excitation for accurately assessing the tumor heterogeneity *in situ* and *ex vivo*.

For preparing SPNs, a nanoprecipitation method was utilized by using SP1 or SP2 and DSPE-PEG2k, an amphiphilic polymer that endows SPNs with good water solubility and biocompatibility. They were codissolved in THF and quickly added to water under continuous probe sonication. Once the postprocessing steps were completed, they led to clear nanoparticle solutions (Figure S1a-c) and were used as such for further physicochemical and optical characterizations. The  $\zeta$ -potential measurements of SPN1 and SPN2 were measured to be -38 and -26 mV, respectively (Figure S 1d). The hydrodynamic diameters of SPN1 and SPN2 were measured using dynamic light scattering (DLS) showing a similar size range of  $\sim 60-70$ nm for both (Figure S1e,f). The transmission electron microscopy (TEM) images in the insets revealed their sizes to be slightly smaller (by  $\sim 10-15$  nm), possibly due to the removal of the hydration layer once the samples are prepared for TEM analysis. SPNs were stable at 4 °C as no visible precipitation or deterioration was observed from the colloidal suspension over 2 weeks.

The optical properties of SPNs were measured in PBS1x buffer (pH 7.4). The absorption peaks of SPN1 and SPN2 were 535 and 670 nm, respectively, in accordance with the difference in band gap between the two (Figure S1g). Both SPN1 and SPN2 exhibited an emission peak at 720 and 840 nm, respectively, when both were excited at the same wavelength of 645 nm (Figure S1h). Finally, we collected IVIS images of SPN1 and SPN2 at 645 nm excitation and at different emission wavelengths (680-840 nm). The spectra obtained from the IVIS (Figure S1i) closely resemble the optical spectra obtained from the spectrofluorometer, further indicating that both SPN1 and SPN2 could be excited at a single-laser wavelength. The rationale behind selecting 645 nm (Figures S2 and S3) as the single excitation wavelength for both SPNs over other wavelengths (e.g., 605 or 675 nm) was due to significantly higher emission intensities relative to the other at their corresponding peak emission maxima ( $I_{SPN1}/I_{SPN2}$  at 720 nm  $\approx$ 12, and  $I_{\text{SPN2}}/I_{\text{SPN1}}$  at 840 nm  $\approx$ 14). Such an attribute will be beneficial for using these SPNs in multiplexing in tumormimicking phantoms and ex vivo mouse tumors.

Preparation of RBC-SPNs with Tumor-targeting Capability. As illustrated in Figure S4a, we first extracted the mouse-derived membrane vesicles from RBCs, lipid-inserting them with peptides, and ultimately fusing them (RBC-FA/RBC-cRGD) onto the surface of SPNs, imparting tumor-targetability. In short, RBC ghosts were first derived from purified mouse RBCs via hypotonic treatment and centrifugation steps. Next, RBCm vesicles having a hydrodynamic diameter of 190 nm were prepared with combined bath sonication followed by extrusion through a polycarbonate membrane (Figure S5). Following this, the physical insertion and optimization studies of the ligand-linker-lipid conjugates (DSPE-PEG-cRGD or DSPE-PEG-FA) into the RBCm were conducted in accordance with previous studies to generate functional RBCm, i.e., RBC-FA or RBC-cRGD membranes (Figures S6—S8). Subsequently, these

membranes were mixed with SPNs (SPN1 and SPN2) and extruded to generate tumor-targeted RBC-SPNs (RBC-FA@SPN1 and RBC-cRGD@SPN2).

Stability and Physicochemical, Optical, and Biophysical Characterization of RBC-SPNs. The physicochemical properties of SPNs and RBC-SPNs were systematically investigated. DLS measurements (Figure S4b,c) revealed an average hydrodynamic diameter of 80 nm for RBC-FA@SPN1 and RBC-cRGD@SPN2 with low polydispersity index (PDI) values, indicating their monodisperse nature. The hydrodynamic diameter of RBC-SPNs was slightly larger than SPNs before the RBC membrane coating process. Negative-stained TEM images of SPN1 displayed a uniform spherical shape as expected for such nanoconstructs. For RBC-SPNs, we observed core-shell structures, with the shell to be roughly 8-10 nm, which is in close agreement with the reported width of RBC membranes (Figure S4b-d and S9). In addition, ζ-potential measurements (Figures S4e and S10) showed the reduction in the surface charge for SPN1 and SPN2 upon RBCm coating to -10.8 and -12 mV, respectively. This was close to the  $\zeta$ potential of RBCm only (-11 mV). RBC-SPNs exhibited excellent colloidal stability with no signs of aggregation over 2 weeks (Figure S11). Furthermore, we observed no significant change in optical characteristics in SPNs after the RBC membrane coating process (Figure S4f), including no changes in the molar extinction coefficient (Figure S12) and fluorescence quantum yield of SPNs before and after the RBCm coating process (SPN1 = 2.5%, RBC-SPN1 = 2.4%, SPN2 = 2.8%, and RBC-SPN2 = 2.65%). In addition, RBC-SPNs demonstrated superior photostability than ICG in aqueous solution, evidenced by small fluorescence intensity loss under continuous laser irradiation for 30 min with laser power density of under continuous laser power density of 100 mW/cm<sup>2</sup> (Figure S13).

As lyophilization of nanomaterials has tremendous advantages for their storage and distribution, we demonstrated that the biomimetic coating imparted RBC-SPNs with improved dispersibility as previously shown by us and others. <sup>42</sup> After subjecting RBC-SPNs to the lyophilization process in which they were obtained as powders (Figure S14a), they were stored at 4 °C for 2 weeks. Subsequently, they were redispersed with PBS1x saline in solution, and it did not result in any noticeable change in color prelyophilization. Furthermore, the freezedrying process had a negligible change in the hydrodynamic diameter or the changes in their optical properties (Figure S14b).

We further performed biophysical characterization studies to confirm successful membrane coating on SPNs due to presence of CD47 proteins on the surface of the nanoparticles. CD47 protein is a well-known "marker of self" receptor on the surface of RBC membranes that binds to the signal regulatory protein  $\alpha$ receptors of macrophages to inhibit phagocytic uptake. Consequently, the presence of CD47 on RBCm-coated SPNs would indicate successful functionalization without the loss in activity of the RBCm. Here, different samples including RBCm, SPNs, and RBC-SPNs were mixed with fluorescent antibodies for CD47, and we observed the highest fluorescent signal intensity for RBCm, followed by RBC-SPNs. The SPNs had the weakest signal intensity due to the lack of CD47 receptors on their surface (Figure S4g). We further performed a simple dotblot study to confirm the presence of CD47 protein receptors by using secondary antibodies against CD-47, and it showed the trend as expected: CD-47 was present on RBCm and RBC-SPNs but not on SPNs (Figures S4h,i and S15). SDS-PAGE analysis

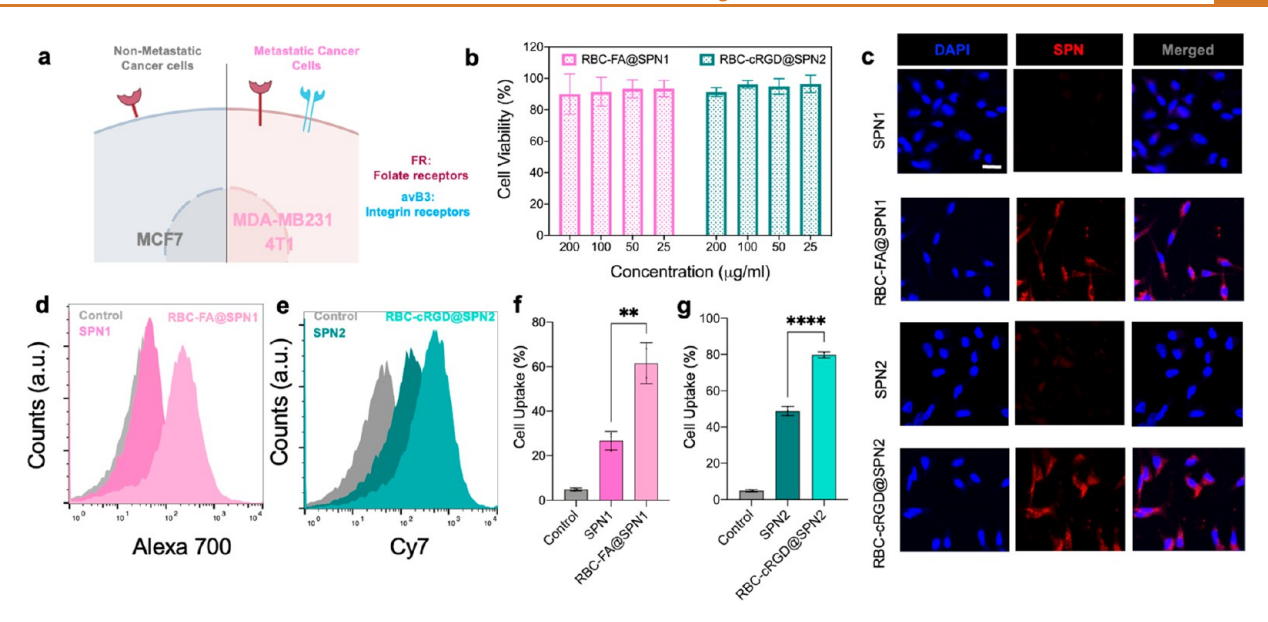


Figure 2. Biological evaluations of RBC-SPNs. (a) Schematic representation of two cell lines, MCF-7, which overexpresses folate receptors, and 4T1, which overexpresses both folate receptors and  $\alpha\nu\beta$ 3 integrin receptors. (b) MTT assay of RBC-SPNs in 4T1 cell lines. (c) Confocal laser scanning microscopy (CLSM) images of SPNs and RBC-SPNs incubated in 4T1 cell lines for 8 h. The red fluorescence indicates the nanoparticles, and cell nuclei (blue) were stained with 4',6-diamidino-2-phenylindole (DAPI). The scale bar shown in white is 10  $\mu$ m. Flow cytometry analysis and corresponding cell uptake percentages for (d and f) SPN1 and RBC-FA@SPN1 and (e and g) SPN2 and RBC-cRGD@SPN2.

showed that the protein profile between the RBCm vesicles and RBC-SPNs did not show any major difference, with the CD-47 protein bands being visible after the coating process (Figures S4j and S16).

In Vitro Cytotoxicity and Cellular Internalization of RBC-SPNs in Cancer Cell Lines. After confirming the successful coating of RBCm on SPNs, we evaluated the in vitro biocompatibility and cellular uptake of the nanoparticles in MCF-7 cells and 4T1 cells. As is the case with SPNs (SPN1 and SPN2), RBC-SPNs also had negligible cytotoxicity against both cell lines, even after incubation at high concentrations of 200  $\mu$ g/ mL (Figure 2a,b and Figure S17). We next tried to evaluate whether our lipid-insertion strategy of imparting RBC-SPNs with tumor-targeting peptides yielded a higher cellular internalization in tumor cell lines expressing the corresponding receptors: MCF-7 cells overexpressing folate receptors but with low expression of  $\alpha v \beta 3$  integrins, 43 and 4T1 cells overexpressing both folate receptors and  $\alpha v \beta 3$  integrins.<sup>44</sup> Based on our confocal laser scanning microscopy (CLSM) imaging of SPNs (SPN1 and SPN2) and RBC-SPNs (RBC-FA@SPN1 and RBC-cRGD@SPN2) incubated in 4T1 cells for 12h, we noticed a higher cellular internalization of the latter as evident by increased red fluorescence (Figure 2c). Contrastingly, for MCF-7 cells, which only overexpresses folate receptors, no observable differences in uptake were noticed for SPN2 or RBC-cRGD@SPN2 due to a lack of  $\alpha v \beta 3$  integrin receptors (Figure S18). RBC-FA@SPN1 on the other hand continued to show a marked increase in cellular uptake over SPN1. We relied on flow cytometry to quantify the cellular uptake of SPNs in the two cell lines used for our CLSM studies. For 4T1 cells, it showed an increase in cellular internalization (Figure 2d-g) of both RBC-FA@SPN1 (62%) and RBC-cRGD @SPN2 (78%) compared to their noncoated and nonlipid inserted counterparts, SPN1 (26%) and SPN2 (48%). For MCF-7 cells, both RBC-cRGD@SPN2 and SPN2 showed similar cellular internalizations (~22% and ~28%) due to a lack

of  $\alpha\nu\beta$ 3 integrins on these cell lines. However, RBC-FA@SPN1 continued to have a higher cellular uptake (~56%) than SPN1 (~18%) due to selective endocytosis uptake *via* the folate receptors.

Reduced Uptake of RBC-SPNs in the Presence of RAW **264.7 Macrophages.** As shown earlier, the RBCm coating retained the bioactivity of the CD47 proteins on the surface of SPNs. Hence, we next attempted to explore if the RBC-SPNs were imparted with the ability to escape from capture by macrophage phagocytosis. SPNs prepared from nanoprecipitation of SP1/SP2 with polymer-lipid conjugates (DSPE-PEG) acted as a control for this experiment, with the lipid coating not having a selective interaction with the macrophages. We incubated SPNs and RBC-SPNs in the mouse macrophage cell lines, RAW 264.7 for 2 and 4 h, respectively (Figure 3a). Two different incubation time points (2 vs 4 h) were selected to show that continuous uptake of RBC-SPNs in RAW 264.7 macrophages is unlikely to occur due to a slower uptake process. Subsequently, the cells were examined using CLSM. The images (Figure 3b) and the subsequent fluorescent intensity analysis at 2 and 4 h (Figure 3c-f) showed strong red fluorescence in the macrophage incubated with SPNs compared to RBC-SPNs. This suggested significant uptake of SPNs by the macrophages, demonstrating that the RBCm coating suppressed the cellular internalization of RBC-SPNs in the RAW 264.7. We further utilized flow cytometry to do quantitative analysis and assessment to corroborate our CLSM data (Figure 3g-j). It was evident that the uptake of SPN1 or SPN2 in RAW 264.7 macrophage cells was significantly higher than RBC-SPN1 or RBC-SPN2, respectively, and gradually increased with longer incubation periods (2h vs 4 h).

Ex Vivo Tissue Penetration and Tissue Phantom Experiments. Understanding how the signal from RBC-FA@ SPN1 and RBC-cRGD@SPN2 changes when the tumor is embedded below normal tissues would be important for its clinical translation. To investigate how these nanoparticles

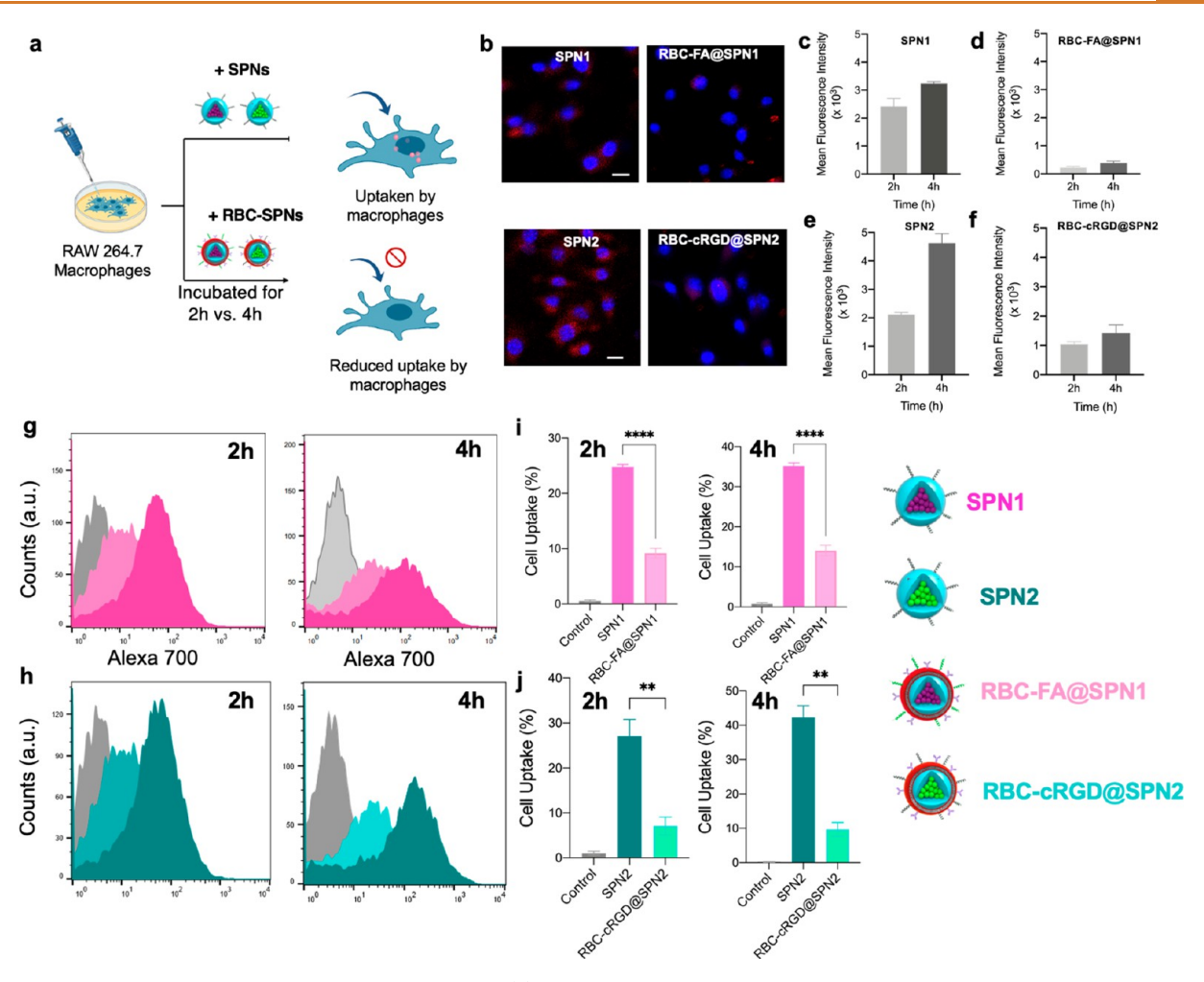


Figure 3. Uptake of RAW 264.7 macrophages by RBC-SPNs. (a) Schematic representation of reduced uptake of RBC-SPNs compared to SPNs. (b) Representative confocal laser scanning microscopy (CLSM) images of SPNs and RBC-SPNs incubated in RAW 264.7 macrophage cell lines for 4 h (scale bar:  $10 \mu m$ ), and (c-f) their corresponding fluorescent intensity comparisons at t=2 h and t=4 h. (h-j) Flow cytometry experiments were conducted for SPNs vs RBC-SPNs at t=2 h and t=4 h, with their corresponding cell uptake percentages calculated for each of the two-time points.

behave in different types of tissue, phantom tumor studies were conducted. A set of phantom tumors were prepared with a 100 μL concentration of RBC-FA@SPN1 and RBC-cRGD@SPN2 dispersed in 1% (by weight) agarose gel (Figure S19a-d). These phantom tumor gels were covered by pork fat, muscle, and skin of different thicknesses and imaged using the IVIS. Fluorescence signal intensity at the region of interest was measured. Figure S19c-k shows how the fluorescence signal attenuates when different widths of pork muscle and fat is placed on the RBC-FA@SPN1 phantom tumor gels. We observed that the fluorescence signal was reduced by 60% for RBC-FA@SPN1 with 2 mm of fat tissue on top. The signal was further reduced by 78% with 4 mm fat and by 90% with 6 mm fat tissue. RBCcRGD@SPN2 lost 50% signal with 2 mm fat, 78% with 4 mm fat, and 90% with 6 mm fat. SPN2 having more red-shifted emission exhibited better penetration of 2 mm of fat, but the fluorescence signals were trivial when imaged with 4 and 6 mm of fat. When tested with 2 mm muscle tissues, RBC-FA@SPN1 phantom tumors lost ~80% of the signal. With 4 and 6 mm muscle tissues on top, the signal loss further increased to 86% and 88%, respectively. RBC-cRGD@SPN2 phantom tumors lost 58% signal with 2 mm muscle on top, which increased to 70% and 75% signal with 4 and 6 mm muscle on top, respectively. SPN2

being red-shifted helps with improved fluorescence signals due to enhanced signal penetration depth in muscle tissues. To investigate the signal penetration of SPNs on the epidermis, we further placed 4 mm pork skin on top of the gels. RBC-FA@ SPN1 phantom tumor gels lost 80% of the signal, while RBCcRGD@SPN2 lost 85% of the signal. Figure S20 also shows representative IVIS fluorescence images of signal from RBCcRGD@SPN2 phantom tumor gel with different thicknesses of pork muscle tissues on top. Such signal loss through the skin tissues will not pose any significant issue as most FIGS are open surgeries. In a typical procedure, these imaging probes are first injected, and after a stipulated time, the surgeons make one large cut where skin is first removed, exposing the tumor and a minimal number of healthy tissues. The optical signals from the accumulated dyes in the tumors are collected using camera sensors in the operating suite guiding the surgeons in making the resection. These experiments provide insight as to how tissues on top of the tumor phantom attenuated the fluorescence signals drastically and that SPN2 having more red-shifted emission than SPN1 provides a better tissue penetration depth response.

**Extended** *in Vivo* **Blood Circulation of RBC-SPNs.** Next, we investigated the effect of RBCm coating on improving the circulation time of the SPNs in the blood as demonstrated in

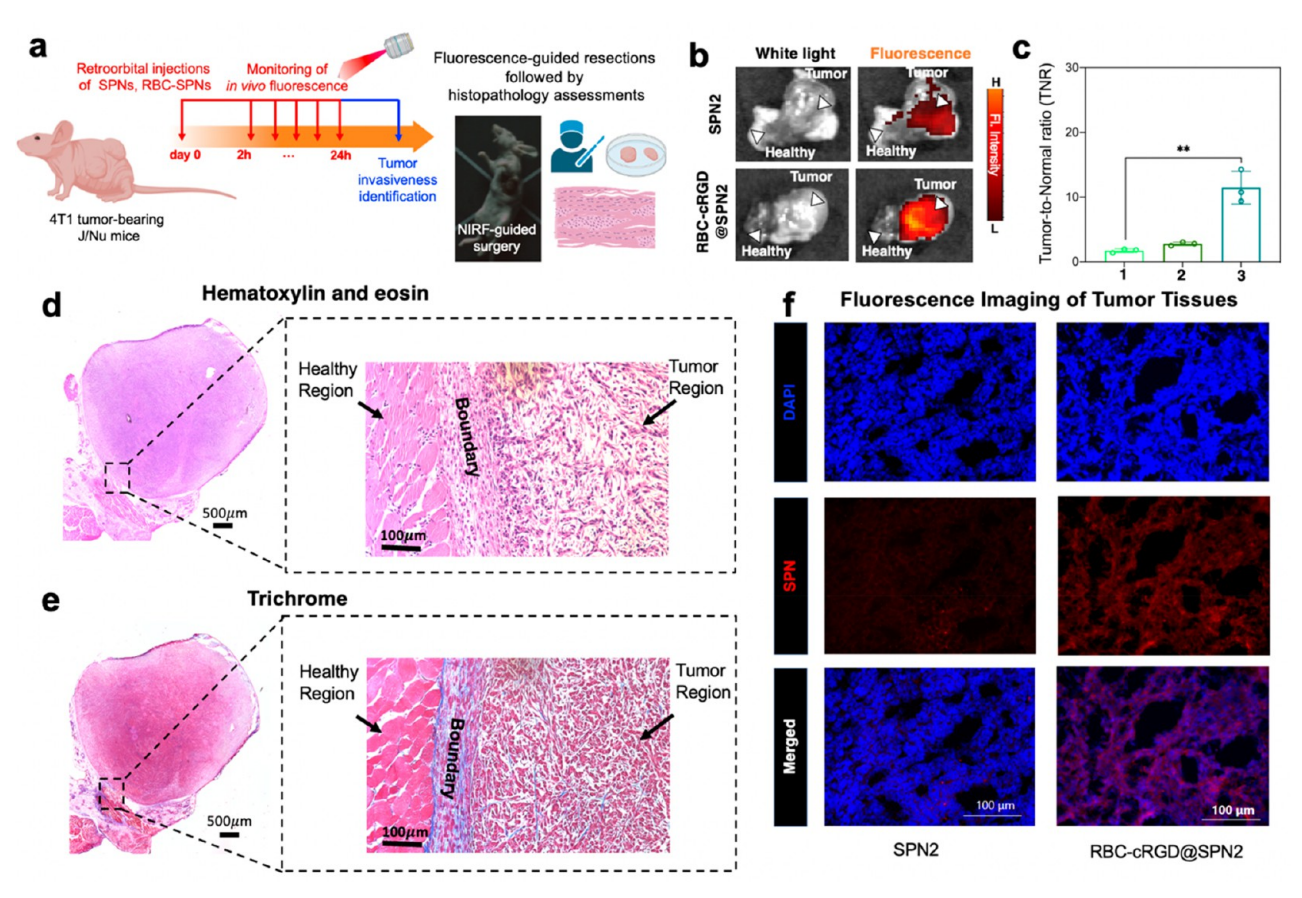


Figure 4. Tumor delineation identification for fluorescence-guided surgical intervention. (a) Schematic illustration showing *in vivo* and *ex vivo* accumulation in 4T1 tumor-bearing mouse models wherein surgical resections were conducted followed by histopathological assessments. (b) Fluorescence images were acquired for resected sections to highlight fluorescent areas (tumor region) and nonfluorescent areas (healthy regions). (c) Semiquantitative analysis of ROI from tumor and normal tissues in subcutaneous 4T1 tumor-bearing mice at 24 h postinjection was collected for (1) SPN2, (2) RBC-SPN2, and (3) RBC-cRGD@SPN2. Histopathology assessments of tissue slices were conducted *via* (d) hematoxylin and eosin, and (e) trichrome staining to highlight the tumor region, boundary, and healthy region. (f) Fluorescence images of tissue specimens surgically resected were acquired. Cell nuclei were stained with DAPI. The images were acquired at the NIR channel 670–750 nm with an excitation at 650  $\pm$  22.5 nm. Scale bar: 100  $\mu$ m.

other nanoparticle platforms. <sup>45–48</sup> The strain of rats used for the in vivo study was the same as the rat strain we derived our RBCm to avoid any potential immune responses that may arise from the inconformity in the blood cell type, a highly desired feature for clinical translation. Balb/c mice were injected with SPNs (without any RBCm coating) and RBC-SPNs via the retroorbital route (Figure S20a). Upon systemic administration, all plasma samples exhibited a strong fluorescence signal at 0.5 h, indicating the presence of a high concentration of SPNs and RBC-SPNs in the systemic circulation (Figure S20b,c). The fluorescence gradually decreased over time due to the clearance of the nanoparticles by the liver and kidneys. However, we observed a significant difference in mean fluorescence intensity between SPNs and RBC-SPNs starting at 6 h postadministration. As a result, no fluorescence was detected in mice with SPNs, whereas about ~20% relative fluorescence was retained in those with RBC-SPNs, showing the beneficial role of RBCmcoating in extending the systemic circulation of the nanoparticles. No noticeable difference was observed between RBC-SPN-1 and RBC-SPN-2 in the absence of tumors.

Improved *in Vivo* and *ex Vivo* Delineation of Tumors using Receptor-Specific RBC-SPNs for Surgical Guidance. The accumulation behavior of SPNs and tumor-targeting RBC-SPNs in tumors was first evaluated for their ability in

precise imaging of tumors. Xenograft 4T1 murine breast tumor models were established by inoculating 4T1 cells subcutaneously into the mammary fat pad of nude mice. All mice were fed a chlorophyll-free diet, which did not show any autofluorescence in the body, thereby reducing the background signal at the acquired emission wavelengths (Figure S21). The nanoparticles were administered into the retro-orbital artery of each mouse and the periodic change in mean fluorescence intensity at the tumor site was monitored for 24 h. As shown in Figures S22 and S23, the fluorescence signal at the tumor site gradually increased for both SPNs and RBC-SPNs as time went by. However, RBC-SPNs had significantly higher fluorescence signals than SPNs in all time points due to a combination of enhanced permeability and retention (EPR) effect and active targeting via tumor-targeting peptides. For SPNs, only the EPR effect was responsible for their accumulation in tumors; hence, a slower tumor uptake was observed compared to RBC-SPNs.

Surgical resection is regarded as the primary curative procedure that is commonly utilized for therapeutic interventions of different solid tumors. However, the precise localization of tumor margins is a major intraoperative challenge and often results in tumor recurrence if the residual tumor is left behind. Using these biomimetic, tumor-targeted nanoparticles and precision guidance from NIR fluorescence imaging,

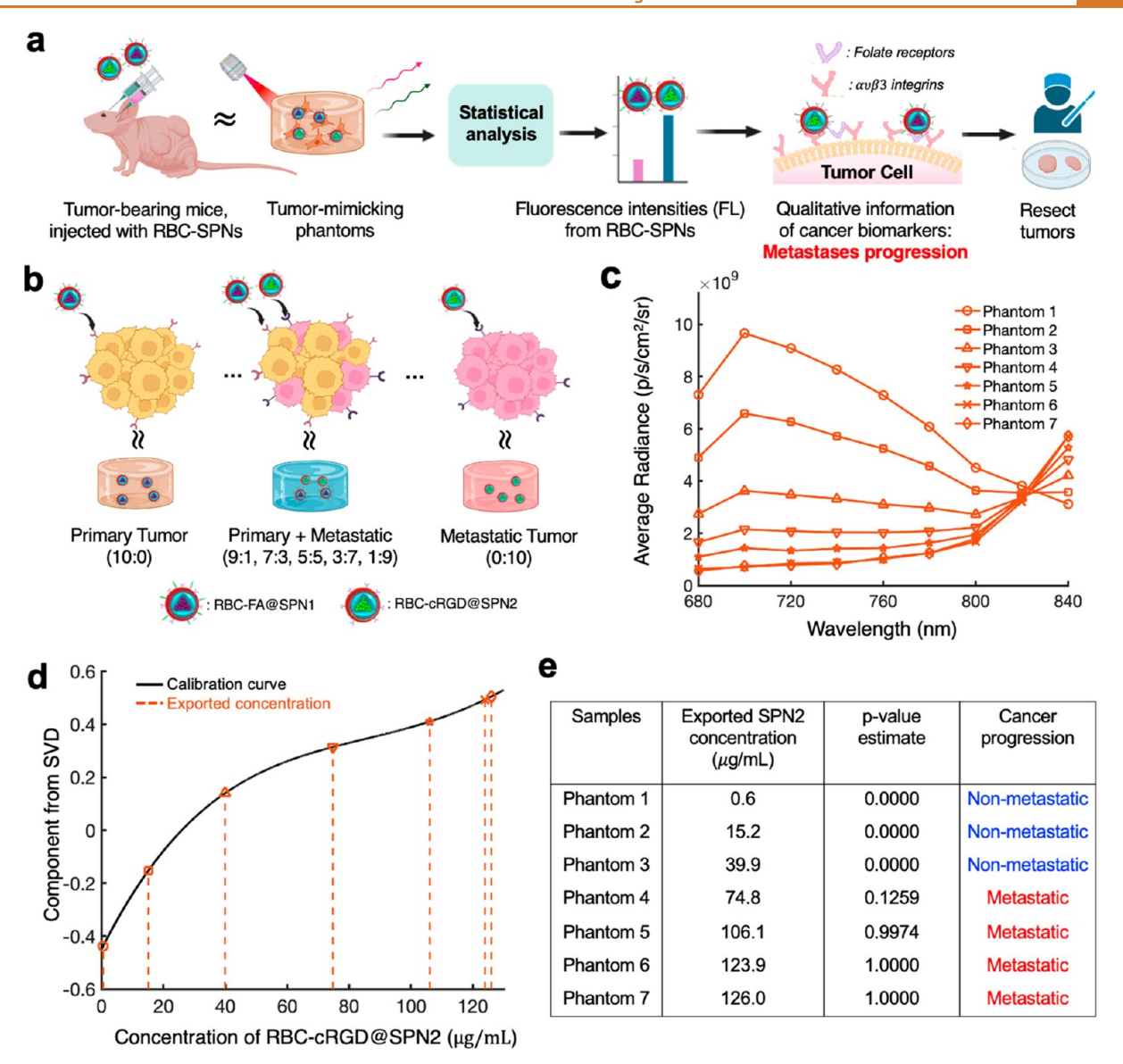


Figure 5. Prediction of cancer progression in tumor-mimicking phantoms using biomimetic nanoparticles and statistical tools. (a) Schematic workflow of tumor-mimicking phantom samples (akin to mice-derived tumors in terms of their optics) determines the concentration of two RBC-SPNs, correlating to qualitative expression levels of cancer biomarkers. This would aid in the surgical decision-making process. (b) Both RBC-FA@SPN1 and RBC-cRGD@SPN2 mixed in different volume/volume ratios to mimic the cancer progression from primary tumors to highly metastatic tumor. (c) Fluorescent spectra acquired from the IVIS from seven different tumor-mimicking phantoms at unknown concentrations of two RBC-SPNs at excitation wavelength of 640 nm and emission wavelength ranging from 680 to 840 nm. (d) Localizing SVD components from phantom samples on the calibration curve to obtain the concentration of RBC-cRGD@SN2. For the calibration curve, see Figure.S29. (e) Obtained concentration of RBC-cRGD@SN2 from the calibration curve of known phantoms and p-value estimate that indicate the cancer progression as metastatic or nonmetastatic.

complete debulking of tumors was performed at 24 h as a proof-of-concept study (Figure 4a). RBC-SPNs had extended blood circulation shown earlier; hence, attempting this study at a later stage postinjection (at 24 h) will be beneficial as the fluorescence signal was highest in the tumors and surrounding tissues exhibited only negligible fluorescence signal as shown in Figure 4b. This contributed to a very high tumor-to-normal tissue (T/NT) ratio (~11) for RBC-cRGD@SPN2 (Figure 4c), which is higher than the Rose criterion <sup>49</sup> of 5, showcasing their potential as imaging agents for fluorescence-guided surgical resections. Both SPNs and RBC-SPNs had appreciable but significantly lower T/NT ratios of 1.6 and 2.95, respectively, than the tumor-specific counterpart at the same dose. To further visualize the tumor margins and successful debulking of tumors, tissue

specimens containing both the tumor and normal tissues were histologically analyzed by hematoxylin and eosin (H&E) staining and trichrome staining. The stained tissue specimens displayed distinct malignant tumorous regions adjacent to normal healthy regions separated by a boundary region, which was distinguishable in terms of their cellular morphology and distribution of nuclei (Figure 4d,e). The corresponding tumor tissue specimens were also visualized using fluorescence microscopy after staining them with 4′,6-diamidino-2-phenylindole (DAPI) to visualize the cellular nucleus. The red fluorescence signals emitted from the nanoparticles were used to indicate their accumulation in tumors. Immunofluorescence (IF) images were also acquired by staining the tumor slices with antibodies specific to the biomarkers being investigated in this

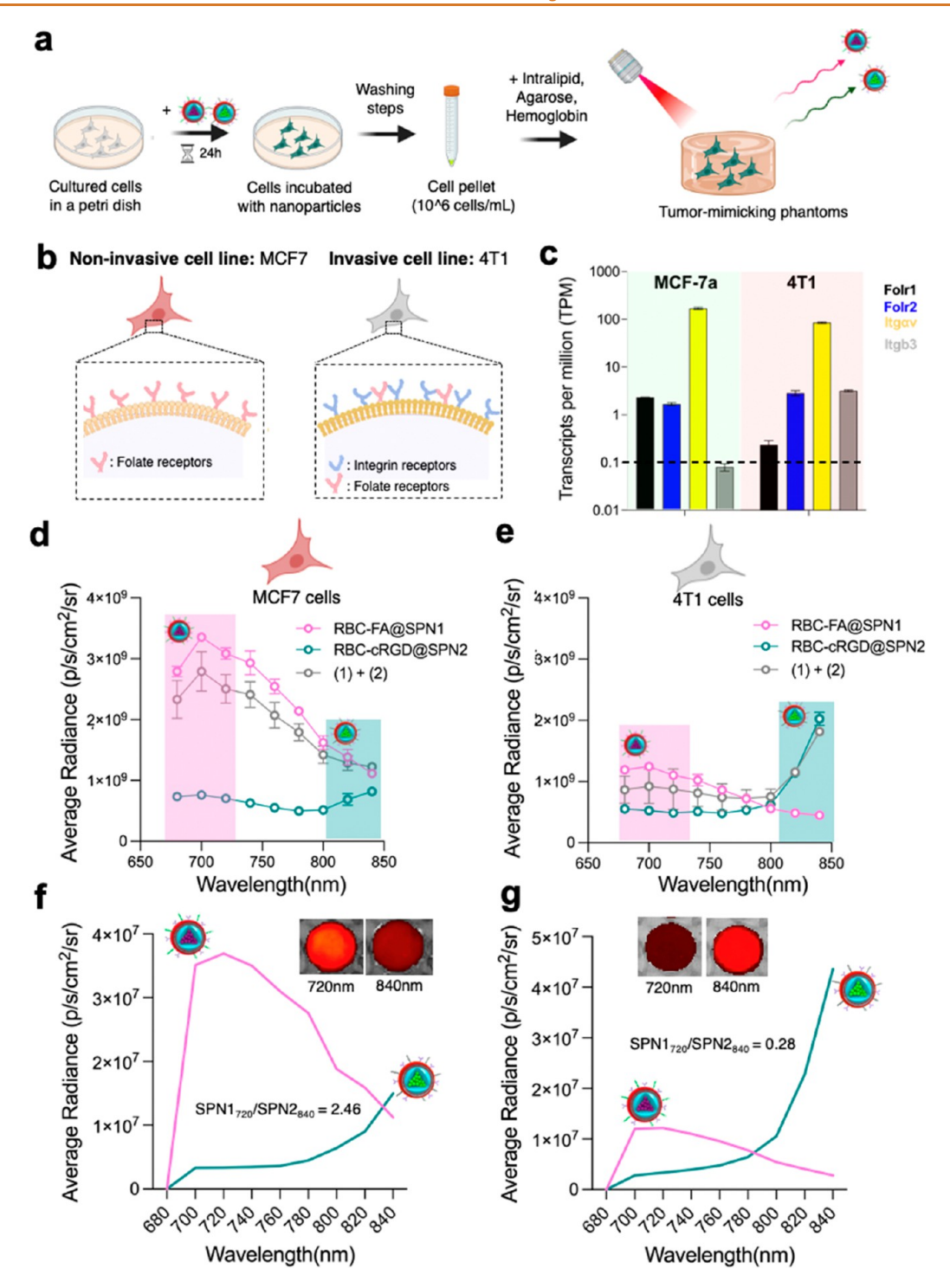


Figure 6. Prediction of cancer progression in noninvasive and invasive tumor-mimicking phantoms using biomimetic nanoparticles. (a) Schematic representation of preparing tumor-mimicking phantoms composed of nanoparticles internalized into either noninvasive or invasive tumor cells mixed with intralipid, agarose, and hemoglobin. (b) Representative noninvasive tumor cell line (MCF-7a) expressing folate receptors and invasive tumor cell line (4T1) expressing both folate receptors and integrin ανβ3 were selected for preparing the phantoms. (c) RNA sequencing data confirming the biomarker expressions in MCF-7a and 4T1 tumor cells. Fluorescent spectra were collected from (d) MCF-7 tumor phantoms and (e) 4T1 tumor phantoms wherein RBC-FA@SPN1, RBC-cRGD@SPN1, or RBC-FA@SPN1+RBC-cRGD@SPN2 were treated with respective tumor cells for 24 h. (f and g) Corresponding unmixing of fluorescence intensities in RBC-FA@SPN1+RBC-cRGD@SPN2 revealed differential signals of RBC-FA@SPN1 and RBC-cRGD@SPN2 for MCF-7 and 4T1 tumor phantoms, indicating distinctive biomarker expression in each tumor cell line.

study (folate,  $\alpha v \beta 3$  integrin) in the EGFP channel (Figure S24). As evident, RBC-cRGD@SPN2 had higher accumulation in tumors than SPN2 (Figure 4f), closely agreeing with a trend from our *ex vivo* and *in vivo* fluorescence imaging studies. IF

images further supplemented these findings due to the overlap between nanoparticle accumulation and different biomarkers. These collective results reported here demonstrate the potential of tumor specific SPNs to detect tumor margins in an operating room and enable the precise differentiation of contrast signals between the tumor and the normal healthy regions of the specimen. Such a biomimetic nanoparticle agent could provide meaningful data to surgeons in the operating room.

At 24 h postinjection of SPNs and tumor-targeted RBC-SPNs, the mice were sacrificed to resect major organs (such as liver, spleen, heart, and kidneys) and tumors. Based on the *ex vivo* fluorescence imaging of major organs, both SPNs and RBC-SPNs were detected in the liver, kidneys, and spleen (in addition to the tumors), indicating that these are the main pathways of clearance for SPNs. Interestingly, the accumulation of RBC-SPNs in the liver was significantly lower than in SPNs, demonstrating the efficacy of RBCm coating in reducing liver uptake (Figure S25).

Qualitative Biomarker Estimation and Predicting Tumor Metastases at Single Excitation Wavelength. As our understanding of tumor heterogeneity has increased over the past decade, it is evident that there are multiple cancer biomarkers expressed on the cell surface of many solid tumors. Such findings further iterate an unmet need to transition from traditional single-biomarker approaches currently used in clinics<sup>50,51</sup> to the ones that target multiple cancer biomarkers. Using a single-biomarker approach often leads to subjective decision-making and variable outcomes resulting in incomplete tumor resections. 52,53 This could be further augmented by the ability to visualize multiple biomarkers to get an idea of the cancer progression (such as metastases spread). Furthermore, accurately assessing the distribution of multiple fluorophores at single-wavelength excitation is advantageous, as multiple excitations for each fluorophore often results in tedious imaging instrumentations in the operating rooms. Allowing surgeons to have portable devices such as fluorescence imaging sensors<sup>13</sup> that can precisely phenotype heterogeneous cancer in real-time with high specificity, sensitivity, and resolution could provide better tumor delineation without the need for secondary surgeries and, consequently, better patient health. At present, however, there is a lack of availability of such cancer-targeted probes and/or fluorescence-based multiplexing tools that could be used in an intraoperative setting capable of being excited at a single wavelength.

Toward this aim, we have demonstrated the efficacy of using our two spectrally tuned biomimetic nanoparticles as a multiplexed detection tool for cancer progression in  $ex\ vivo$  tumor-mimicking phantoms and  $in\ vivo$  tumor-bearing mice. Our two biomimetic nanoparticles can be excited at a single wavelength (640 nm) with distinct emission peak maxima (720 and 840 nm) and target two distinct cell-surface tumor biomarkers (folate, primary cancer;  $\alpha v \beta 3$  integrin, metastasis). Extracting individual fluorescence intensities from the two biomimetic nanoparticles can provide us with a more qualitative assessment of tumor progression, improved guidance during the surgical resection process ( $in\ situ$  and  $ex\ vivo$ ), and an accurate decision-making process in an operating suite. We further validated our findings of metastases spread with RNA sequencing results and fluorescence imaging of tumor slices.

First, we developed tumor-mimicking phantoms that comprised agarose, hemoglobin (Hb), and intralipid solution. These *ex vivo* phantoms have been shown to closely mimic solid tumors in terms of tissue optics. <sup>54–56</sup> The two biomimetic nanoparticles were mixed in different volume-by-volume (v/v) ratios to account for a variable expression level of the cancer biomarkers (folate and  $\alpha v \beta 3$  integrin) in a solid tumor, which would correspond to cancer progression (Figure 5a,b).

Phantoms having only RBC-FA@SPN1 were used to mimic primary cancer having extensive folate receptor expression (10:0). A phantom having only RBC-cRGD@SPN2 was used to mimic metastatic tumors with very high  $\alpha\nu\beta$ 3 integrins expressions (0:10). Phantoms having variable v/v ratios of RBC-FA@SPN1 and RBC-cRGD@SPN2 (9:1, 7:3, 5:5, 3:7, 1:9) were used to mimic the gradual increase of cancer progression from primary cancer to a metastatic one. To obtain the calibration curve for this study, tumor phantoms with known ratios of the two biomimetic nanoparticles were excited at 640 nm and emission spectra were collected from 680 to 840 nm using the IVIS (Figure S26).

To corroborate the validity of our SVD analysis above, we tested its efficacy in predicting the concentration of RBC-SPNs using a single-blinded experiment with seven tumor-mimicking phantoms with unknown mixtures of the two RBC-SPNs. A qualitative understanding of the two probes in a tumor could provide insights into biomarker expression and cancer progression (metastases), thereby guiding surgeons with the resection process of solid tumors. To acquire the concentration of two RBC-SPNs in tumor-mimicking phantoms, similar imaging and decomposition analysis processes were performed (Figure S26). Seven tumor-mimicking phantom samples were taken and excited with a 640 nm laser. Emission fluorescence between 680 and 840 nm with 20 nm intervals was collected and plotted as original spectra (Figure 5c). After performing SVD analysis on the original spectra, the first two terms of SVD results were able to reconstruct the original spectra with an accuracy of 98.1% (Figure S27). By locating the second term of the Eigen combination V value on the calibration curve, the unknown concentrations of RBC-cRGD@SNP2 and RBC-FA@SPN1 were determined with comparable (98%) accuracy (Figure 5d,e and Table S1). We further calculated p-value estimates classifying tumor phantoms as either metastatic or nonmetastatic tumors, with a p-value <0.01 being considered significant. Such estimators would help surgeons in the intervention procedure and potentially assist in making surgical decisions such as resection of metastatic tumors.

We next attempted to use our two biomimetic nanoparticles to predict the cancer progression in noninvasive and invasive tumor-mimicking phantoms. Unlike the previous case where we used a solution containing agarose, intralipid, and hemoglobin to make phantoms, we further included tumor cells labeled with nanoparticles (Figure 6a). For noninvasive tumor phantoms, we used a representative cancer cell line (MCF-7a), and for invasive tumor phantoms, we used a representative cancer cell line (4T1). Each of these cells was labeled with either (i) RBC-FA@ SPN1, (ii) RBC-cRGD@SPN2, or (iii) RBC-FA@SPN1 + RBC-cRGD@SPN2. MCF-7a cells overexpress folate receptors but have low expressions of  $\alpha v \beta 3$  integrin, <sup>43</sup> and 4T1 cells overexpress both folate receptors and  $\alpha v \beta 3$  integrin (Figure 6b). 44 RNA sequencing data from MCF-7a and 4T1 tumor cells were used to get an estimate of different receptor expressions (Figure 6c). Subsequently, fluorescence imaging of phantoms was conducted using an IVIS imager to obtain their emission spectra. For MCF-7a tumor phantoms, there was strong emission intensity at 720 nm both with RBC-FA@SPN1 nanoparticles alone and in mixtures, indicating their strong internalization due to specific targeting of folate receptors (Figure 6d). RBC-cRGD@SPN2 labeled MCF7 cell phantoms showed weaker emission intensity at 840 nm and thus lower uptake. An opposite trend was observed for 4T1 tumor phantoms, with strong emission intensity at 840 nm for both

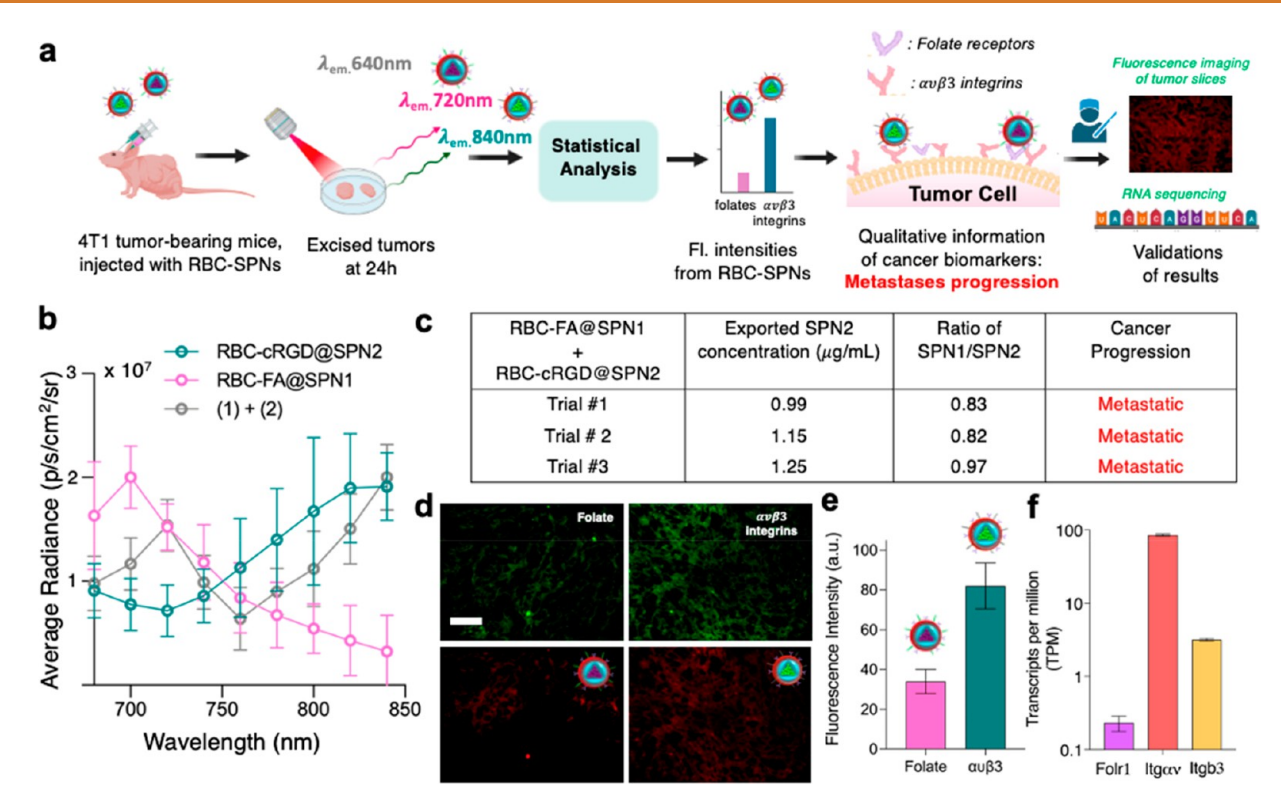


Figure 7. Prediction of cancer progression in preclinical tumor models using biomimetic nanoparticles and statistical tools. (a) Schematic workflow of 4T1-tumor bearing mice models injected with two RBC-SPNs and correlating to qualitative expression levels of cancer biomarkers. This will be further verified *via* fluorescence imaging of tumor tissues and RNA-sequencing. (b) Fluorescence emission of *ex vivo* tumors (n = 4 tumors) where the mice were injected with RBC-FA@SPN1 (pink), RBC-cRGD@SPN2 (green), and both RBC-FA@SPN1 and RBC-cRGD@SPN2 (gray). (c) Obtained concentration of RBC-cRGD@SPN2 from the calibration curve after SVD calculations, corresponding ratio of [SPN1]/[SPN2] calculation, and indication of cancer progression. (d) Top panel: Immunofluorescence (IF) images of tumor tissues injected with the nanoparticle mixture labeled with antibodies for folate and  $\alpha\nu\beta$ 3 integrin. Bottom panel: Fluorescence imaging to show RBC-FA@SPN1 and RBC-cRGD@SP2 accumulation in tumors. (e) Corresponding fluorescence intensity calculations. (f) RNA transcriptome analysis of 4T1 tumors indicating the expression levels of folr1,  $\alpha\nu$ , and  $\beta$ 3.

RBC-cRGD@SPN2 nanoparticles alone and in mixtures, indicating their strong internalization by specifically targeting the  $\alpha v \beta 3$  integrins (Figure 6e). RBC-FA@SPN1 labeled 4T1 cell phantoms showed weaker emission intensity at 720 nm and consequently lower uptake. Both MCF7 and 4T1 tumor cell phantoms labeled with a mixture of biomimetic nanoparticles were spectrally unmixed to quantify the contributions from individual biomimetic nanoparticles (RBC-FA@SPN1 and RBC-cRGD@SPN2). From the unmixing in MCF-7a tumor cell phantoms, RBC-FA@SPN1 had a higher contribution than RBC-cRGD@SPN2 (SPN1 emission at 720/SPN2 emission at 840 = 2.46), indicating an overabundance of folate receptors on MCF-7a cells utilized by the latter for cellular internalization (Figure 6f). Contrastingly, from unmixing the mixture of biomimetic nanoparticles in 4T1 tumor cell phantoms, RBCcRGD@SPN2 had a higher contribution than RBC-FA@SPN1 (SPN1 emission at 720/SPN2 emission at 840 = 0.28), suggesting that  $\alpha v \beta 3$  integrins were utilized for cellular internalization by the former (Figure 6g). These unmixing results closely agree with the trends obtained from our RNA sequencing data in Figure 6c.

We next attempted to confirm this multiplexed detection capability in *in vivo* tumor-bearing mouse models. 4T1 cells were selected as a representative case for highly tumorigenic, invasive, and metastatic ( $\alpha v \beta 3$  integrin  $\gg$  folate) tumors (Figure 7a). However, one critical issue needs to be addressed before proceeding to multiplexed detection experiments. It is well

understood that active-targeted nanoparticles (such as RBC-FA@SPN1 and RBC-cRGD@SPN2) utilize a combination of both active-targeting mechanisms and passive uptake mechanism (EPR) for the uptake behaviors in solid tumors. 57-61 This could interfere with our molecular phenotyping and qualitative biomarker estimation studies in in vivo subjects, and thus, the following corrections were made. 4T1-tumor-bearing mice (n =3 tumors each) were injected separately with (i) nontumor targeted nanoparticles (RBC-SPN1 and RBC-SPN2) where only the EPR effect was dominant and (ii) tumor-targeted nanoparticles (RBC-FA@SPN1 and RBC-cRGD@SPN2), which utilizes both the EPR effect and active targeting. At 24 h, when the EPR effect is the least predominant and the active targeting mechanism is dominant, the fluorescent signals at tumor locations were acquired and plotted against the emission wavelength (Figure S30). Assuming the EPR effect and active targeting are the only two uptake pathways of nanoparticles into solid tumors, we subtracted the contribution of the EPR effect from the emission spectra.

Using singular value decomposition (SVD), we analyzed the tumor spectra of nanoparticles employing "EPR effect only" and "EPR + active targeting" and quantified the contribution of the EPR effect. After plotting the tumor data, we found the fluorescent signal coming from EPR to be linearly dependent on the total fluorescent intensity. SVD being a linear decomposition technique, EPR, therefore, did not change the eigen spectra but only scaled the singular value. The scaling factor was very similar

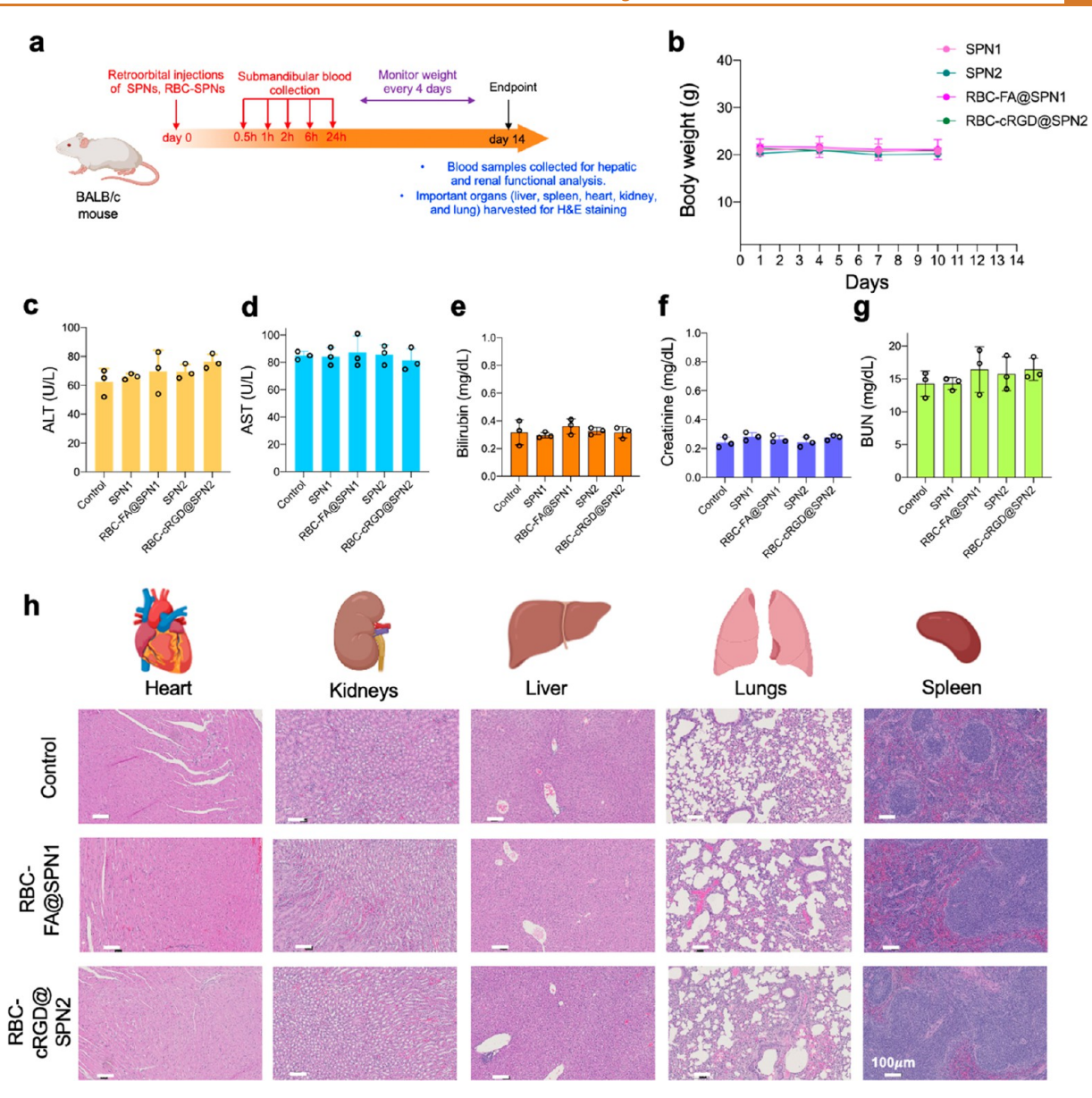


Figure 8. In vivo toxicity evaluation of RBC-SPNs by body weight measurements, blood tests and histology analysis. (a) Schematic explanation of retro-orbital injection of BALB/c mice with injections of SPNs and RBC-SPNs, (b) followed by the mice body weight changes over a span of 2 weeks. Blood biochemistry data were collected including several liver function biomarkers, (c) ALT and (d) AST, and kidney function biomarkers, (e) Creatinine, (f) BUN, and (g) Bilirubin. (h) Representative H&E-stained images of major organs from the euthanized mice on the day 14th after being retro-orbital injected with saline or RBC-SPNs.

for both SPN1 and SPN2, demonstrating that their ratio is robust to EPR background effects. Thus, SVD will reduce the contribution of unwanted signals when the result is expressed as an SPN1/SPN2 ratio. The resulting emission spectra, which only incorporated contributions of active-targeting components, i.e., folate,  $\alpha v \beta 3$  integrin, respectively, were subsequently used for our molecular phenotyping and qualitative biomarker estimation experiments (Figure 7b). The emission spectra from tumor tissues that were injected with the nanoparticle mixture were corrected for scattering and SVD analysis was adapted to obtain the concentration of each nanoparticle in the tumor (Figures S31-S33). A ratio of SPN1/SPN2 less than 1 indicated more accumulation of SPN2 into the tumor than SPN1, suggesting a greater amount of  $\alpha v \beta 3$  integrin than foliate. The emission spectra from tumor tissues injected with the mixture were also fitted with a linear combination of the vial

spectra of individual SPNs (Figures S28 and S29). The ratio of the fitting parameters was used to estimate the relative distribution of the biomarkers. A ratio less than 1 (~0.86) indicates the lesser accumulation of RBC-FA@SPN1 than RBCcRGD@SPN2 (Figure.S33), indirectly suggesting more  $\alpha v \beta 3$ integrin than folate. To validate our qualitative estimation of biomarkers from our statistical analysis, we utilized both fluorescence microscopy images of tumor tissues and RNA sequencing (RNA-seq) data. 4T1-tumor-bearing mice that were injected with both RBC-SPNs for this multiplexed study were sacrificed, and the tumor tissues obtained were imaged under fluorescence microscopy (Figure 7d). Two adjacent tissue slices from the tumor injected with the mixture were stained with antibodies corresponding to folate and  $\alpha v \beta 3$  integrin, respectively (Figure 7d, top panel). The folate antibody-stained slice was imaged in the Cy5 NIR fluorescence channel to

visualize the uptake of RBC-FA@SPN1 while the  $\alpha v\beta 3$  integrins antibody-stained tumor slice was imaged in the ICG NIR fluorescence channel to visualize the uptake of RBC-cRGD@SPN2. Based on the semiquantitative analysis, a stronger and more persistent NIR signal was distributed across the tumor tissues for RBC-cRGD@SPN2 than RBC-FA@SPN1 (Figure 7e). This trend was further validated by RNA-seq data, which showed that the distribution levels of both  $\alpha v$  and  $\beta 3$  integrins were significantly higher than Folr1 (folate- $\alpha$ ) receptors (Figure 7f), indicating more accumulation of RBC-cRGD@SPN2 (targeting  $\alpha v\beta 3$  integrins) than RBC-FA@SPN1 (targeting folate- $\alpha$  receptors).

**Preclinical Evaluations of RBC-SPNs.** As for any experimental nanoparticle, there is always a cause for concern about the potential *in vivo* toxicity. We proceeded to do a full-scale toxicity study as we will be leveraging an RBCm-coated nanoparticles platform, which could cause potential toxicity issues including transfusion reactions due to a mismatch of the blood types, potentially leading to fatal incidents.

For our study, BALB/c mice (n = 3) received a retro-orbital injection of 200 µL of PBS1x or PBS containing SPNs or RBC-SPNs at a concentration of 1 mg/mL. The body weight of mice was monitored for 2 weeks as it is a direct indicator of the in vivo toxicity of the nanoparticles. There were no significant changes in the body weight of the mice for either the control or the treated group postinjection. Furthermore, none of the animals experienced severe symptoms or death, suggesting potentially no in vivo side effects (Figure 8a-c). On day 14 of the injection, all mice were euthanized, the major organs including hearts, kidneys, livers, lungs, and spleens were collected for H&E staining, and their blood was collected for a blood test. We observed no hepatic or renal toxicity that was induced by these nanoparticles as shown by the normal values of the liver function markers, i.e., ALT, AST (Figure 8d,e), and kidney function markers, i.e., Creatinine, BUN, and Bilirubin (Figure 8f-h). These values were consistent with those in the control group that had been injected with saline. In addition to that, no observable sign of major organ damage was noticed from the H&E staining, implying negligible hepatic and hematological toxicity of the RBC-SPNs. We further conducted an erythrocyte hemolysis assay experiment to evaluate the interactions of RBC-SPNs and red blood cells derived from BALB/c mice. As shown in Figure S34, the RBC-SPNs exhibited minimum hemolysis at all tested concentrations for RBC-SPN1 and RBC-SPN2 (10-200  $\mu$ g/mL). These results collectively indicate that RBCm camouflaged SPNs have no noticeable in vivo toxicity to healthy mice, at least at our tested dose, and are suitable for in vivo applications. However, more work is needed to systematically study the response of short- and long-term toxicity of these nanoparticles at various doses.

While imaging systems like PerkinElmer's IVIS spectrum have become essential tools for the preclinical researcher, their reliance on a filter wheel that can pick out just a single wavelength at any given time makes them unsuited for the dynamic activity that is intrinsic to the clinical environment. As such, there is a need to design not only fluorescent probes that can emit at different wavelengths, even when excited at a single wavelength, but also fluorescent imaging systems that can discriminate between those emission wavelengths from the information captured in a single snapshot. A solution is posed by an 18-band snapshot hyperspectral imaging system that was previously evaluated for sentinel lymph node dissection with multiple near-infrared fluorophores but is equally applicable for

tumor detection with a collection of cancer biomarkers. <sup>62</sup> By permitting multiple wavelengths to be probed at each pixel, this snapshot hyperspectral imaging system preserves the high frame rates that are possible with color imaging systems while facilitating a balance between field of view and spatial resolution that has been demonstrated with similarly constructed imaging systems. <sup>63,64</sup> These features enable the imaging system to capture more information at a faster rate than laboratory instruments without sacrificing the benefit of image fidelity that is offered by those instruments. Spectral unmixing of two RBC-SPNs was conducted using an 18-band snapshot hyperspectral imaging system designed for near-infrared fluorescence imageguided surgery (Figure S35).

## **CONCLUSION**

In summary, we have introduced a biomimetic nanoplatform having favorable biological properties (increased biocompatibility, prolonged in vivo blood circulation and reduced liver uptake) and spectral properties (providing specific and robust fluorescence enhancement in tumors with T/NT tissue ratios ~11 and multiplexed molecular phenotyping at single-wavelength-excitation). Such features of the nanoparticle contrast agent will account for the tumor heterogeneity issues that are often associated with solid tumors and provide tumor biomarker expressions and cancer progression (such as metastases) to surgeons in an operating room. We validated these features using in vitro cells, in vivo and ex vivo tumor-bearing mice models, and ex vivo tumor phantom models. As the EPR effect in humans has been found to be variable unlike in mice models, more in-depth studies need to be conducted that enable patientspecific stratification of EPR with corresponding adjustments to our SVD model. However, such efforts are beyond the current emphasis of this study, which discusses murine and phantom models. Our biomimetic nanoplatform with favorable biological and spectral properties results in applications for precise fluorescence-guided surgical interventions in preclinical studies on a wide range of solid tumor models.

# **METHODS**

**Materials.** All materials were purchased from Sigma-Aldrich and used without any modifications unless stated separately. Agarose was purchased from Fisher Scientific. Pork skin, fat, and muscle tissues were acquired from local grocery stores.

**Preparation of SPNs.** For preparing SPN1 or SPN2, 0.5 mg of SP1/SP2 and 5 mg of DSPE-mPEG2000 were dissolved in 1 mL of THF by stirring it for 2 min. This was followed by a dropwise addition of 9 mL of DI water in an empty 20 mL vial under probe sonication for 3:30 min. Subsequently, THF was removed by stirring at 300 rpm at room temperature overnight with nitrogen flushing gently. The mixed solution was ultrafiltered at 4500 rpm for 30 min and then washed three times with DI water to remove any excess DSPE-mPEG2000. The final products (SPN1 and SPN2) were collected and stored at 4 °C.

**Preparation of RBCm.** RBCs derived from BALB/C mouse blood were purchased directly from BioIVT. Subsequently, it was subjected to hemolysis where the RBCs were suspended in lysis buffer, *i.e.*,  $0.25 \times PBS$  at 4 °C for 1 h. The resulting solution was centrifuged 4 times at 20 000g to eliminate hemoglobin until a pink pellet (RBCm concentrate) was obtained, and the supernatant solution was colorless. The pink pellet was resuspended in distilled water ( $\sim 50$  mL) and vigorously mixed and sonicated for 10 min in an ice—water mixture followed by extrusion through a 200 nm polycarbonate membrane 15 times using a mini extruder (Avanti Polar Lipids). The final RBCM solution was stored at -80 °C under further use.

Preparation of Targeting Peptide Inserted RBCms. RBCm obtained in the previous step was taken and incubated with  $100 \, \mu g/mL$ 

DSPE-PEG-FA or DSPE-PEG-cRGD at 37  $^{\circ}$ C for 30 min to form RBC-FA and RBC-cRGD, respectively. All samples were centrifuged at 700g for 10 min and washed with PBS1x twice before reconstructing them into vesicles using the mini extruder.

Preparation of RBC-FA@SPN1 and RBC-cRGD@SPN2. RBC-FA and RBC-cRGD modified membranes were subsequently coated onto the SPNs that were prepared earlier by extruding through 200 nm polycarbonate porous membranes using the mini extruder 15 times. Hydrodynamic diameter and ζ-potential measurements were collected (Zetasizer Nano ZS, Malvern Instruments Ltd.).

Transmission Electron Microscopy (TEM) Imaging of RBC-SPNs and SPNs. A drop of RBCm-coated or bare (non-RBC-coated) nanoparticle solution was deposited onto a glow-discharged, carbon-coated TEM grid and incubated for 5 min. Excess liquid was removed, and samples were dried overnight in a desiccation chamber. For negative staining, samples were stained with 1% uranyl acetate for 30 s immediately before imaging. All samples were imaged using a JEOL JEM-2100 Cryo transmission electron microscope at 200 kV.

Physicochemical, Optical, and Molecular Biology Characterization of SPNs and RBC-SPNs. Dynamic light scattering (DLS) measurements were conducted to measure the hydrodynamic size distribution (intensity average) of the nanoparticles on a Malvern Zetasizer ZS90 instrument (Malvern Instruments Ltd.) at a fixed angle of 90°. ζ-Potential values were determined using a Malvern Zetasizer (Malvern Instruments Ltd.) of Nano series. Ultraviolet-visible (UVvis) absorbance was recorded on a GENESYSTM 10S UV-vis spectrophotometer (Thermo Scientific). Absorbance spectra were collected at an interval of 1 nm scanning from 300 to 1000 nm. To evaluate the presence of CD47 on the surface of the particle, allophycocyanin-labeled antimouse CD47 antibody was used (BioLegend, San Diego, CA) according to a previously established protocol. The protocol to conduct the Dot blot studies was conducted from a previous study against CD47 proteins on RBC membranes. Further protein characterization was conducted using a sodium dodecyl sulfate polyacrylamide gel electrophoresis (SDS-PAGE) method that has been previously reported. Briefly, the samples were heated at 95 °C for 10 min, and 20  $\mu$ L of each sample was loaded in each well for a 10% SDS-PAGE gel. Samples were run at 100 V for 2 h, and the obtained gel was stained with Coomassie blue, washed with deionized water, and subsequently imaged.

**Calculation of Quantum Yields of SPNs and RBCm-SPNs.** Using ICG as the reference, the quantum yields of SPN1, SPN2, RBC-SPN1, and RBC-SPN2 were calculated using the following formula:  $Q = Q_{\rm ICG} \times I \times {\rm OD}_{\rm ICG} \times N^2/(I_{\rm ICG} \times {\rm OD} \times N_{\rm ICG})$ , where Q is the fluorescence quantum yield, I is the integrated fluorescence intensity, N is the refractive index of solvent (PBS), and OD is the optical density (absorption).  $Q_{\rm ICG}$  in PBS is 0.027.

Dispersion Stability of RBC-SPNs against Lyophilization. RBC-SPNs stock solutions were taken in glass vials (2 mL). The resulting solutions were frozen by placing them in liquid nitrogen for a few minutes and then connected immediately to a freeze-drier (-47 °C) with an applied vacuum ( $53 \times 10^{-4}$  mbar) for  $\sim$ 24 h. The freeze-dried products were reconstituted with deionized water (1 mL). The RBC-SPN solutions were briefly sonicated and analyzed using DLS and IVIS fluorescence imager.

**MTT Assay of RBC-SPNs.** The cytotoxic effects of various samples (SPN1, SPN2, RBC-FA@SPN1, RBC-cRGD@SPN2) in two different cell lines (MDA-MB231, MCF7) were investigated using a MTT assay established previously.  $^{38}$ 

*In Vitro* Cellular Uptake Experiments. MCF-7 and 4T1 cancer cells were cultured in a 6-well plate (10<sup>5</sup> cells/well) and incubated with DMEM containing SPN1, SPN2, RBC-FA@SPN1, and RBC-cRGD@SPN2 at a concentration of 50  $\mu$ g/mL for 12 h. The treated cells were subsequently washed, stained with DAPI, and then fixed. LSM 880 confocal laser scanning microscopy (Carl Zeiss) was used to capture the fluorescence images.

Flow cytometry was further performed to quantify the cellular uptake. 4T1 and MCF-7 cancer cells were incubated with SPNs and tumor-targeted RBC-SPNs at a concentration of 50  $\mu$ g/mL for 12 h. Then, the treated cells were successively washed with PBS1x,

trypsinized, collected, and resuspended in 1% FBS in PBS solution and used for cellular uptake analysis on a BD LSR Fortessa.

In Vitro Macrophage Experiments. RAW 264.7 macrophage cells were cultured in a 6-well plate ( $10^5$  cells/well) and incubated with DMEM containing SPN1, SPN2, RBC-FA@SPN1, and RBC-cRGD@SPN2 at a concentration of 50  $\mu$ g/mL for 2 and 4 h, respectively. The treated cells were subsequently washed, stained with DAPI, and then fixed. LSM 880 confocal laser scanning microscopy (Carl Zeiss) was used to capture the fluorescence images.

Flow cytometry was further performed to quantify the cellular uptake. RAW 264.7 macrophage cells were incubated with SPNs and tumor-targeted RBC-SPNs at a concentration of  $50 \,\mu\text{g/mL}$  for 2 and 4 h, respectively. Then, the treated cells were successively washed with PBS1x, trypsinized, collected, and resuspended in 1% FBS in PBS solution and used for cellular uptake analysis on a BD LSR Fortessa.

Ex Vivo Tissue Penetration Experiments. Synthesized RBC-FA@SPN1 and RBC-cRGD@SPN2 after ultracentrifugation were dispersed in PBS 1x buffer with a concentration of 400  $\mu$ g/mL. One wt % agarose aqueous solution was heated until full dissolution. Prepared solutions of RBC-FA@SPN1 and RBC-cRGD@SPN2 were mixed with 1 wt % agarose aqueous solution with a final nanoparticle concentration of 100  $\mu$ g/mL. The mixture was quickly transferred into a 12-well tissue culture plate for gel formation. The plate was left at room temperature until SPN-agarose gel completely cooled and then was solidified. The RBC-SPN-agarose gels were carefully removed from the 12-well plate with an approximate thickness of 1-1.5 cm. The tissue phantom imaging was carried out by a PerkinElmer IVIS Spectrum CT in Vivo Imaging System (Waltham, MA). Pork fat and muscle tissues were sliced into 2, 4, 6, 8, and 10 mm sections. The prepared pork tissues with various thicknesses were placed on top of the SPN-agarose gels in the imaging compartment of the IVIS. SPN-agarose gel covered by 4 mm pork muscle tissue and pork skin on the top was also imaged for comparison. Fluorescence images at each tissue thickness for both SPNs were acquired with similar settings from the *in vivo* imaging by the IVIS. Agarose was purchased from Fisher Scientific. Pork skin, fat, and muscle tissues were acquired from local grocery stores.

**Ex Vivo Phantom Experiments.** We made phantom tumors with agarose, hemoglobin (Hb), and intralipid solution to make more realistic models for imaging. For SPN agarose-Hb-intralipid gel, we mixed an equal volume of RBC-SPN with a solution of 2% agar with hemoglobin and intralipid. For a 3 mL solution of gel, we mixed 30 mg of agarose, 15 mg of hemoglobin, 75 μL of intralipid solution (20%), and 1425 μL of PBS. Then, the solution was heated to 60 °C and 1.5 mL of a 200 μL RBC-SPN solution was added. The solution was cooled to 4 °C for 2 h to form the gel. The subsequent tumor phantoms made from RBC-FA@SPN1 and RBC-cRGD@SPN2, respectively, were imaged on the IVIS with single excitation of 675 nm, Em. 720 nm and Em. 840

Animal and Tumor Models. Female mice BALB/c and J:NU of 22-25 g weight (2 months old) were purchased from Jackson Laboratory (Bar Harbor, ME). Upon arrival, all mice were housed in the animal care facility at the Beckman Institute for Advanced Science and Technology (University of Illinois at Urbana-Champaign, Urbana, IL) under the required conditions with free access to water and food throughout the experiments. All animal studies were performed in accordance with the guidelines of the Institutional Animal Care and Use Committee (IACUC, Protocol ID 20194) and the Division of Animal Resources at the University of Illinois. Breast cancer xenograft was established using a 4T1 murine mammary carcinoma cell line (CRL-2539, ATCC, Manassas, VA). An 100  $\mu$ L 4T1 cell solution (10<sup>6</sup> cells per injection) was administered at the mammary fat pad of the second nipple of the left side of each J:NU mouse using a 27G1/2 needle. Anesthesia was maintained by mask inhalation of 1.5-2.0% isoflurane throughout the procedure.

**Tumor-Cell-Mimicking Phantom Models.** MCF-7a and 4T1 cancer cells were cultured in Petri dishes until 80% confluency, following which they were incubated with DMEM containing SPN1, SPN2, RBC-FA@SPN1, RBC-cRGD@SPN2, or both (50:50 v/v ratio) at a concentration of 200  $\mu$ g/mL for 24 h. Subsequently, after the washing steps, the cells labeled with nanoparticles (10<sup>6</sup> cells) were taken

to form the tumor-cell-mimicking phantoms. For making the phantoms, we mixed these cells with agarose, hemoglobin (Hb), and intralipid solution. For making MCF-7 or 4T1 tumor cell-mimicking phantoms, we mixed 1 mL of cells labeled nanoparticles with a solution of 2% agar with hemoglobin and intralipid. For a 3 mL solution of gel, we mixed 30 mg of agarose, 15 mg of hemoglobin, 75  $\mu$ L of intralipid solution (20%), and 1425  $\mu$ L of PBS. Then, the solution was heated to 37 °C and 1 mL of cell labeled nanoparticles solution was added. The solution was cooled to 4 °C for 2 h to form the gel. The subsequent tumor phantoms made were imaged on the IVIS with single excitation of 640 nm and emission ranging from 680 to 840 nm.

*In Vivo* Blood Circulation Studies. To investigate the circulation time of the nanoparticles, dye-labeled SPNs and RBC-SPNs (1000  $\mu$ g/mL) were administered into the retro-orbital sinus of BALB/c mice. At 0.5, 1, 2, 6, and 24 h after nanoparticle administration, 20  $\mu$ L of blood was collected from the submandibular vein of each mouse and centrifuged at 2000g for 10 min to separate the plasma. The samples were stored at -80 °C and imaged with the IVIS.

The body weights for each mouse were recorded using a digital scale every 3 days. After waiting for 2 weeks, all mice were euthanized to harvest the organs (heart, liver, kidney, spleen), which were histologically analyzed for any sign of chronic cytotoxicity from the nanoparticles. Prior to sacrificing the mice, their blood was also collected for analyzing their liver and kidney function assessments. Mice administered with PBS were used as a negative control.

*In Vivo* Fluorescence Imaging. When the 4T1 tumor size reached approximately 10 mm, the mice were randomly assigned to administer SPNs and RBC-SPNs into the retro-orbital sinus at a dose of mg/kg (n = 3) and imaged with the IVIS at 2, 4, 8, 12, and 24 h.

**Histological Analysis.** After the mice were imaged using the IVIS and euthanized, the tissues of the main organs including tumors were obtained and studied using hematoxylin and eosin stain using the standard protocol. The fixed tumors and tissues were first dehydrated using ethanol solution, followed by embedding in paraffin and cutting into sections with a thickness of  $10~\mu m$ . The sections were washed with ethanol and immersed in hematoxylin working solution for 3 min and then in eosin working solution for 1 min. The stained slices were washed with water and observed by a Keyence microscope BZ-800E.

For fluorescence imaging of tumor slices, the collected tumor tissues were first dehydrated and then embedded in a frozen optimal cutting temperature medium and cut into 10  $\mu \rm m$  using a cryostat (Leica, CM1950). These sections were washed with PBS1x three times followed by staining with DAPI at 25 °C for 20 min, followed by staining with folate-specific and  $\alpha v \beta 3$  integrin-specific antibodies that were imaged in the EGFP channel. The stained sections were observed under a Keyence microscope BZ-800E. For SPN1 fluorescence, a Cy5 filter was used. For SPN2 fluorescence, an ICG filter was used.

**Statistical Analysis.** The results of experiments are reported as the mean  $\pm$  standard deviation. The experimental data for *in vitro* and *in vivo* experiments in each group were analyzed by ANOVA with *post hoc* tests using GraphPad Prism 8 software. Different significance levels of the data were considered at \*p < 0.05, \*\*p < 0.01, and \*\*\*p < 0.001.

Tumor Phantom Fluorescent Spectra Analysis. Fluorescent spectra were analyzed and plotted using MATLAB. RBC-FA@SPN1 and RBC-cRGD@SPN2 were mixed in different v/v combinations: RBC-FA/RBC-cRGD = 130:0, 117:13, 91:39, 65:65, 39:91, 13:117, and 0:130  $\mu$ g/mL. The emission spectra were collected from 680 to 840 nm with 20 nm intervals by exciting the mixture at 655 nm. With nine wavelength points and seven different v/v combinations, the emission spectra were rewritten as a matrix  $A_{9\times7}$ . Singular value decomposition was performed on the spectra  $A_{9\times7}$  and decomposed it into  $U_{9\times7}$ ,  $S_{7\times7}$ , and  $V_{7\times7}$ , where  $A = USV^{T}$ . The first two terms of U, S, and V were used to reconstruct the spectra,  $A \approx U_{9\times 2}S_{2\times 2}V_{2\times 2}^{T}$ . The calibration curve was obtained by rescaling the  $V_2$  with the absolute intensity value and replotted it as a function of different v/v combinations. For samples with unknown concentration of the two RBC-SPNs, the study was conducted in a single-blind manner. Each sample was excited at 640 nm and collected emission fluorescence from 680 to 840 nm, and the collected spectra were decomposed using the same SVD analysis. The  $V_2$  value from the decomposition was highlighted on the calibration

curve to calculate the estimated RBC-cRGD@SPN2 (and consequently, RBC-FA@SPN1) concentrations.

Microcentrifuge Tube Fluorescent Spectra Analysis. An 18band snapshot hyperspectral imaging system was constructed from a stacked photodiode image sensor and a three-by-three-pixel spectral filter array and was then equipped with a 647 nm long-pass filter (BLP01-647R, Semrock) as described in ref 62; it was further configured with a Rokinon 50 mm f/1.4 lens adjusted to an aperture of f/2.8 and two notch filters at 658 nm (NF03-658E, Semrock) and 785 nm (NF03-785E, Semrock) for this particular study. Fluorescence images of any samples were captured under 665 nm laser excitation (BWF2-665, B&W Tek) provided by a beam-expanded and currentcontrolled source that was configured to an irradiance of 20.7 mW/cm<sup>2</sup> at the location of the sample, while white light images of any samples were captured under direct halogen lamp illumination (OSL1 w/ OSL1B bulb, Thorlabs). The 665 nm laser was setup at an angle of  $105^{\circ}$ with respect to the sample and the imaging system, while the halogen lamp was setup at an angle of  $20-30^{\circ}$  with respect to the same.

The spectra of RBC-FA@SPN1 and RBC-cRGD@SPN2 were determined by extrapolating the spectra observed across various concentrations of SPN1 or SPN2 (in solution with phosphate buffered serum) to a unit concentration of SPN1 or SPN2 (Supporting Information). The spectral unmixing of RBC-FA@SPN1 and RBCcRGD@SPN2 was then evaluated by decomposing the spectra observed for various mixtures of SPN1 and SPN2 (again in solution with phosphate buffered serum) into a concentration-weighted linear combination of the spectra of SPN1 and SPN2 (Supporting Information). Since the emission from SPN1 could excite SPN2, the ratios found via unmixing were biased away from SPN1 toward SPN2 whenever the SPNs were mixed. To counteract this coupling between the SPNs, a calibration curve that mapped the observed (biased) ratios to the actual (unbiased) ratios was defined as a scaled, shifted, and clamped version of a square root function before being fitted and applied to the data (Supporting Information).

## ASSOCIATED CONTENT

# Supporting Information

The Supporting Information is available free of charge at https://pubs.acs.org/doi/10.1021/acsnano.3c00578.

Figures of synthesis and characterization of SPNs, excitation spectra of SPNs, excitation wavelength optimizations, hydrodynamic diameter, polydispersity index values, and  $\zeta$ -potential measurements, lipidinsertion optimization, titration curve of absorbance vs concentration, negative-stained TEM images, long-term stability, molar extinction coefficient calculations, photostability measurements, lyophilization studies, dot blot studies, polyacrylamide gel electrophoresis studies, cell viability for nanoparticles in MCF7 cell line, flow cytometry histograms showing uptake of nanoparticles in MCF7 cells, ex vivo tissue depth penetration and tissue phantom experiments, in vivo circulation lifetime studies, in vivo time-dependent fluorescence of mice with 4T1 tumors, quantification of fluorescence intensities of tumor regions as a function of postinjection time, immunofluorescence images discriminating normal and tumor regions, ex vivo biodistribution of SPNs and RBC-SPNs, calibration curve in phantoms from SVD analysis, reconstructed spectra from SVD, in vivo fluorescence images of tumor regions acquired using IVIS, fluorescence emission spectra of SPNs in vials at varying concentrations, fluorescence emission spectra of SPNs in ex vivo tumors and corresponding SVD and linear fitting analysis, hemolysis measurements, and spectral unmixing of RBC-SPNs using camera sensors, table of calculated SPN1 concentrations in tumor-mimicking phantoms obtained ACS Nano www.acsnano.org Article

from the calibration curve, and discussions of singular value decomposition methods and spectral unmixing analysis using camera sensors (PDF)

#### **AUTHOR INFORMATION**

### **Corresponding Authors**

Indrajit Srivastava — Department of Bioengineering and Department of Electrical & Computer Engineering, University of Illinois at Urbana—Champaign, Urbana, Illinois 61801, United States; Occid.org/0000-0002-6864-0202; Email: indrajit@illinois.edu

Shuming Nie — Department of Bioengineering, Department of Electrical & Computer Engineering, Department of Chemistry, and Carle Illinois College of Medicine, University of Illinois at Urbana—Champaign, Urbana, Illinois 61801, United States; orcid.org/0000-0002-7328-1144; Email: nies@illinois.edu

Viktor Gruev — Department of Bioengineering, Department of Electrical & Computer Engineering, and Carle Illinois College of Medicine, University of Illinois at Urbana—Champaign, Urbana, Illinois 61801, United States; orcid.org/0000-0003-1280-7971; Email: vgruev@illinois.edu

#### Authors

Benjamin Lew — Department of Electrical & Computer Engineering, University of Illinois at Urbana—Champaign, Urbana, Illinois 61801, United States; orcid.org/0000-0002-4555-0378

Yuhan Wang — Department of Chemistry, University of Illinois at Urbana—Champaign, Urbana, Illinois 61801, United States

Steven Blair – Department of Electrical & Computer Engineering, University of Illinois at Urbana–Champaign, Urbana, Illinois 61801, United States; orcid.org/0000-0002-2505-6866

**Mebin Babu George** – Department of Electrical & Computer Engineering, University of Illinois at Urbana–Champaign, Urbana, Illinois 61801, United States

Brianna Scheid Hajek — Department of Electrical & Computer Engineering, University of Illinois at Urbana—Champaign, Urbana, Illinois 61801, United States

Sushant Bangru – Department of Cell Biology, Duke University, Durham, North Carolina 27705, United States

Subhendu Pandit — Department of Chemistry, University of Illinois at Urbana—Champaign, Urbana, Illinois 61801, United States; Occid.org/0000-0002-4542-2069

Ziwen Wang — Department of Bioengineering, University of Illinois at Urbana—Champaign, Urbana, Illinois 61801, United States

Jamie Ludwig — Division of Animal Resources, University of Illinois at Urbana—Champaign, Urbana, Illinois 61801, United States

Kristen Flatt – Materials Research Laboratories Central Research Facilities, University of Illinois at Urbana–Champaign, Urbana, Illinois 61801, United States

Martin Gruebele — Department of Chemistry and Carle Illinois College of Medicine, University of Illinois at Urbana—Champaign, Urbana, Illinois 61801, United States; orcid.org/0000-0001-9291-8123

Complete contact information is available at: https://pubs.acs.org/10.1021/acsnano.3c00578

#### **Author Contributions**

I.S. conceived the conceptual design and overall experimental design of the study, performed SPN synthesis, optimization, and characterizations, performed and optimized the RBCM coating process and lipid-insertion studies, conducted in vitro studies, and analyzed the data. S.Ba. assisted in data collection for in vitro studies. S.P. prepared tumor phantoms for the study. S.P. and Z.W. performed the tissue penetration experiments via IVIS imaging and analyzed the data. B.L., I.S., M.B.G., and B.S.H. designed the in vivo studies. B.L., M.B.G., B.S.H., J.L., and I.S. conducted in vivo studies. B.L. and I.S. analyzed the data collected from in vivo studies. B.S.H. and I.S. collected and analyzed H&E, trichrome, and fluorescent images of tumor slides. S.Ba. performed the liver and kidney enzyme studies. I.S. collected tumor phantom data using IVIS, Y.W. performed the multiplexed molecular imaging analysis in tumor-mimicking phantoms using SVD, and M.G. assisted with SVD data analysis, supervised the study, and edited the paper. S.Bl. designed, collected, and analyzed the data for multiplexed imaging experiments in microcentrifuge tubes using an image-guided imaging sensor currently undergoing clinical studies. S.N. and V.G. were involved in funding acquisition and supervised the overall project. I.S. wrote the first draft of the manuscript with further inputs from all the authors. All authors have given approval for the final version of the manuscript.

#### Notes

The authors declare no competing financial interest.

#### **ACKNOWLEDGMENTS**

S.N. acknowledges the Grainger College of Engineering and the University of Illinois at Urbana-Champaign for institutional support. V.G. thanks the Congressionally Directed Medical Research Program (grant W81XWH-19-1-0299) and the National Science Foundation (grant 2030421). V.G. and S.N. were supported by National Institute of Health (1P01CA254859). M.G. and Y.W. were supported by NSF MCB-2205665. The authors thank Suyue Lyu for her help in running dot-blot studies and polyacrylamide gel electrophoresis experiments, Nickel Liang for data collection in multiplexing study, and Karen Doty for preparing tumor histopathology and immunofluorescent slides. The authors thank Wilson Poon for discussion and feedback on the manuscript. Transmission electron microscopy and dark-field microscopy imaging were carried out in the Materials Research Laboratory Central Research Facilities, University of Illinois.

# **REFERENCES**

- (1) Brouwer de Koning, S. G.; Vrancken Peeters, M.-J. T. F. D.; Jóźwiak, K.; Bhairosing, P. A.; Ruers, T. J. M. Tumor Resection Margin Definitions in Breast-Conserving Surgery: Systematic Review and Meta-analysis of the Current Literature. *Clinical Breast Cancer* **2018**, *18* (4), e595—e600.
- (2) Lukasiewicz, S.; Czeczelewski, M.; Forma, A.; Baj, J.; Sitarz, R.; Stanislawek, A. Breast cancer epidemiology, risk Factors, classification, prognostic markers, and current treatment strategies an updated review. *Cancers (Basel)* **2021**, *13* (17), 4287.
- (3) Siegel, R. L.; Miller, K. D.; Fuchs, H. E.; Jemal, A. Cancer statistics, 2022. CA: A Cancer Journal for Clinicians 2022, 72 (1), 7–33.
- (4) Frangioni, J. V. New technologies for human cancer imaging. *J. Clin. Oncol*, **2008**, 26 (24), 4012–4021.
- (5) Low, P. S.; Singhal, S.; Srinivasarao, M. Fluorescence-guided surgery of cancer: applications, tools and perspectives. *Curr. Opin Chem. Biol.* **2018**, *45*, 64–72.

- (6) Vahrmeijer, A. L.; Hutteman, M.; van der Vorst, J. R.; van de Velde, C. J. H.; Frangioni, J. V. Image-guided cancer surgery using near-infrared fluorescence. *Nature Reviews Clinical Oncology* **2013**, *10* (9), 507–518.
- (7) van Manen, L.; Handgraaf, H. J. M.; Diana, M.; Dijkstra, J.; Ishizawa, T.; Vahrmeijer, A. L.; Mieog, J. S. D. A practical guide for the use of indocyanine green and methylene blue in fluorescence-guided abdominal surgery. *J. Surg Oncol* **2018**, *118* (2), 283–300.
- (8) O'Donnell, P. W.; Griffin, A. M.; Eward, W. C.; Sternheim, A.; Catton, C. N.; Chung, P. W.; O'Sullivan, B.; Ferguson, P. C.; Wunder, J. S. The effect of the setting of a positive surgical margin in soft tissue sarcoma. *Cancer* **2014**, *120* (18), 2866–2875.
- (9) Keating, J.; Tchou, J.; Okusanya, O.; Fisher, C.; Batiste, R.; Jiang, J.; Kennedy, G.; Nie, S.; Singhal, S. Identification of breast cancer margins using intraoperative near-infrared imaging. *J. Surg Oncol* **2016**, 113 (5), 508–514.
- (10) Pan, J.; Deng, H.; Hu, S.; Xia, C.; Chen, Y.; Wang, J.; Wang, Y. Real-time surveillance of surgical margins via ICG-based near-infrared fluorescence imaging in patients with OSCC. *World J. Surg. Onc.* **2020**, 18 (1), 96.
- (11) Okusanya, O. T.; DeJesus, E. M.; Jiang, J. X.; Judy, R. P.; Venegas, O. G.; Deshpande, C. G.; Heitjan, D. F.; Nie, S.; Low, P. S.; Singhal, S. Intraoperative molecular imaging can identify lung adenocarcinomas during pulmonary resection. *Journal of Thoracic and Cardiovascular Surgery* 2015, 150 (1), 28–35.
- (12) Barth, C. W.; Gibbs, S. L. Fluorescence Image-Guided Surgery a Perspective on Contrast Agent Development. *Proc. SPIE Int. Soc. Opt. Eng.* **2020**, *11222*, 112220J.
- (13) Blair, S.; Garcia, M.; Davis, T.; Zhu, Z.; Liang, Z.; Konopka, C.; Kauffman, K.; Colanceski, R.; Ferati, I.; Kondov, B.; Stojanoski, S.; Todorovska, M. B.; Dimitrovska, N. T.; Jakupi, N.; Miladinova, D.; Petrusevska, G.; Kondov, G.; Dobrucki, W. L.; Nie, S.; Gruev, V. Hexachromatic bioinspired camera for image-guided cancer surgery. *Sci. Transl. Med.* **2021**, *13* (592), eaaw7067.
- (14) Egloff-Juras, C.; Bezdetnaya, L.; Dolivet, G.; Lassalle, H. P. NIR fluorescence-guided tumor surgery: new strategies for the use of indocyanine green. *Int. J. Nanomedicine* **2019**, *14*, 7823–7838.
- (15) Pogue, B. W.; Rosenthal, E. L.; Achilefu, S.; van Dam, G. M. Perspective review of what is needed for molecular-specific fluorescence-guided surgery. *J. Biomed. Opt* **2018**, 23 (10), 1–9.
- (16) Hong, G.; Antaris, A. L.; Dai, H. Near-infrared fluorophores for biomedical imaging. *Nature Biomedical Engineering* **2017**, *1* (1), 0010.
- (17) Kobayashi, H.; Ogawa, M.; Alford, R.; Choyke, P. L.; Urano, Y. New Strategies for Fluorescent Probe Design in Medical Diagnostic Imaging. *Chem. Rev.* **2010**, *110* (5), 2620–2640.
- (18) Veys, I.; Pop, C.-F.; Barbieux, R.; Moreau, M.; Noterman, D.; De Neubourg, F.; Nogaret, J.-M.; Liberale, G.; Larsimont, D.; Bourgeois, P. ICG fluorescence imaging as a new tool for optimization of pathological evaluation in breast cancer tumors after neoadjuvant chemotherapy. *PloS one* **2018**, *13* (5), e0197857.
- (19) Alander, J. T.; Kaartinen, I.; Laakso, A.; Pätilä, T.; Spillmann, T.; Tuchin, V. V.; Venermo, M.; Välisuo, P. A Review of Indocyanine Green Fluorescent Imaging in Surgery. *International Journal of Biomedical Imaging* **2012**, 2012, 940585.
- (20) Zhu, C.; Liu, L.; Yang, Q.; Lv, F.; Wang, S. Water-Soluble Conjugated Polymers for Imaging, Diagnosis, and Therapy. *Chem. Rev.* **2012**, *112* (8), 4687–4735.
- (21) Li, Y.; Li, Z.; Wang, X.; Liu, F.; Cheng, Y.; Zhang, B.; Shi, D. In vivo cancer targeting and imaging-guided surgery with near infrared-emitting quantum dot bioconjugates. *Theranostics* **2012**, *2* (8), 769–76.
- (22) Shang, W.; Xia, X.; Lu, N.; Gao, P.; Peng, L.; Liu, Y.; Deng, H.; Jiang, J.; Li, Z.; Liu, J. Colourful fluorescence-based carbon dots for tumour imaging-guided nanosurgery. *Nanomedicine: nanotechnology, biology, and medicine* **2022**, *45*, 102583.
- (23) Hill, T. K.; Abdulahad, A.; Kelkar, S. S.; Marini, F. C.; Long, T. E.; Provenzale, J. M.; Mohs, A. M. Indocyanine Green-Loaded Nanoparticles for Image-Guided Tumor Surgery. *Bioconjugate Chem.* **2015**, 26 (2), 294–303.

- (24) Mohs, A. M.; Wang, X.; Goodrich, K. C.; Zong, Y.; Parker, D. L.; Lu, Z.-R. PEG-g-poly(GdDTPA-co-l-cystine): A Biodegradable Macromolecular Blood Pool Contrast Agent for MR Imaging. *Bioconjugate Chem.* **2004**, *15* (6), 1424–1430.
- (25) Lew, B.; George, M.; Blair, S.; Zhu, Z.; Liang, Z.; Ludwig, J.; Kim, C. Y.; Kim, K.; Gruev, V.; Choi, H. Protease-activated indocyanine green nanoprobes for intraoperative NIR fluorescence imaging of primary tumors. *Nanoscale Adv.* **2022**, *4* (19), 4041–4050.
- (26) Wu, C.; Chiu, D. T. Highly Fluorescent Semiconducting Polymer Dots for Biology and Medicine. *Angew. Chem., Int. Ed.* **2013**, 52 (11), 3086–3109.
- (27) Li, J.; Rao, J.; Pu, K. Recent progress on semiconducting polymer nanoparticles for molecular imaging and cancer phototherapy. *Biomaterials* **2018**, *155*, 217–235.
- (28) Li, Y.; Tang, R.; Liu, X.; Gong, J.; Zhao, Z.; Sheng, Z.; Zhang, J.; Li, X.; Niu, G.; Kwok, R. T. K.; Zheng, W.; Jiang, X.; Tang, B. Z. Bright Aggregation-Induced Emission Nanoparticles for Two-Photon Imaging and Localized Compound Therapy of Cancers. *ACS Nano* **2020**, *14* (12), 16840–16853.
- (29) Lyu, Y.; Cui, D.; Sun, H.; Miao, Y.; Duan, H.; Pu, K. Dendronized Semiconducting Polymer as Photothermal Nanocarrier for Remote Activation of Gene Expression. *Angew. Chem., Int. Ed.* **2017**, *56* (31), 9155–9159.
- (30) Zhu, H.; Fang, Y.; Zhen, X.; Wei, N.; Gao, Y.; Luo, K. Q.; Xu, C.; Duan, H.; Ding, D.; Chen, P.; Pu, K. Multilayered semiconducting polymer nanoparticles with enhanced NIR fluorescence for molecular imaging in cells, zebrafish and mice. *Chemical Science* **2016**, 7 (8), 5118–5125.
- (31) Zhen, X.; Zhang, C.; Xie, C.; Miao, Q.; Lim, K. L.; Pu, K. Intraparticle Energy Level Alignment of Semiconducting Polymer Nanoparticles to Amplify Chemiluminescence for Ultrasensitive In Vivo Imaging of Reactive Oxygen Species. ACS Nano 2016, 10 (6), 6400–6409.
- (32) Lyu, Y.; Zeng, J.; Jiang, Y.; Zhen, X.; Wang, T.; Qiu, S.; Lou, X.; Gao, M.; Pu, K. Enhancing Both Biodegradability and Efficacy of Semiconducting Polymer Nanoparticles for Photoacoustic Imaging and Photothermal Therapy. *ACS Nano* **2018**, *12* (2), 1801–1810.
- (33) Fang, R. H.; Kroll, A. V.; Gao, W.; Zhang, L. Cell Membrane Coating Nanotechnology. *Adv. Mater.* **2018**, *30* (23), 1706759.
- (34) Hu, Q.; Sun, W.; Qian, C.; Wang, C.; Bomba, H. N.; Gu, Z. Anticancer Platelet-Mimicking Nanovehicles. *Adv. Mater.* **2015**, 27 (44), 7043–50.
- (35) Yang, R.; Xu, J.; Xu, L.; Sun, X.; Chen, Q.; Zhao, Y.; Peng, R.; Liu, Z. Cancer Cell Membrane-Coated Adjuvant Nanoparticles with Mannose Modification for Effective Anticancer Vaccination. *ACS Nano* 2018, 12 (6), 5121–5129.
- (36) Yu, B.; Goel, S.; Ni, D.; Ellison, P. A.; Siamof, C. M.; Jiang, D.; Cheng, L.; Kang, L.; Yu, F.; Liu, Z.; Barnhart, T. E.; He, Q.; Zhang, H.; Cai, W. Reassembly of (89) Zr-Labeled Cancer Cell Membranes into Multicompartment Membrane-Derived Liposomes for PET-Trackable Tumor-Targeted Theranostics. *Adv. Mater.* **2018**, *30* (13), 1704934.
- (37) Ben-Akiva, E.; Meyer, R. A.; Yu, H.; Smith, J. T.; Pardoll, D. M.; Green, J. J. Biomimetic anisotropic polymeric nanoparticles coated with red blood cell membranes for enhanced circulation and toxin removal. *Sci. Adv.* **2020**, *6* (16), eaay9035.
- (38) Srivastava, I.; Xue, R.; Jones, J.; Rhee, H.; Flatt, K.; Gruev, V.; Nie, S. Biomimetic Surface-Enhanced Raman Scattering Nanoparticles with Improved Dispersibility, Signal Brightness, and Tumor Targeting Functions. *ACS Nano* **2022**, *16* (5), 8051–8063.
- (39) Deng, G.; Peng, X.; Sun, Z.; Zheng, W.; Yu, J.; Du, L.; Chen, H.; Gong, P.; Zhang, P.; Cai, L.; Tang, B. Z. Natural-Killer-Cell-Inspired Nanorobots with Aggregation-Induced Emission Characteristics for Near-Infrared-II Fluorescence-Guided Glioma Theranostics. ACS Nano 2020, 14 (9), 11452–11462.
- (40) Li, J.; Cui, D.; Jiang, Y.; Huang, J.; Cheng, P.; Pu, K. Near-Infrared Photoactivatable Semiconducting Polymer Nanoblockaders for Metastasis-Inhibited Combination Cancer Therapy. *Adv. Mater.* **2019**, *31* (46), 1905091.

- (41) Li, J.; Zhen, X.; Lyu, Y.; Jiang, Y.; Huang, J.; Pu, K. Cell Membrane Coated Semiconducting Polymer Nanoparticles for Enhanced Multimodal Cancer Phototheranostics. *ACS Nano* **2018**, 12 (8), 8520–8530.
- (42) Wang, Z.; Popowski, K. D.; Zhu, D.; de Juan Abad, B. L.; Wang, X.; Liu, M.; Lutz, H.; De Naeyer, N.; DeMarco, C. T.; Denny, T. N.; Dinh, P.-U. C.; Li, Z.; Cheng, K. Exosomes decorated with a recombinant SARS-CoV-2 receptor-binding domain as an inhalable COVID-19 vaccine. *Nature Biomedical Engineering* **2022**, *6* (7), 791–805.
- (43) Feng, D.; Song, Y.; Shi, W.; Li, X.; Ma, H. Distinguishing Folate-Receptor-Positive Cells from Folate-Receptor-Negative Cells Using a Fluorescence Off—On Nanoprobe. *Anal. Chem.* **2013**, *85* (13), *6530*—6535.
- (44) Doolittle, E.; Peiris, P. M.; Doron, G.; Goldberg, A.; Tucci, S.; Rao, S.; Shah, S.; Sylvestre, M.; Govender, P.; Turan, O.; Lee, Z.; Schiemann, W. P.; Karathanasis, E. Spatiotemporal Targeting of a Dual-Ligand Nanoparticle to Cancer Metastasis. *ACS Nano* **2015**, *9* (8), 8012–8021.
- (45) Miao, Y.; Yang, Y.; Guo, L.; Chen, M.; Zhou, X.; Zhao, Y.; Nie, D.; Gan, Y.; Zhang, X. Cell Membrane-Camouflaged Nanocarriers with Biomimetic Deformability of Erythrocytes for Ultralong Circulation and Enhanced Cancer Therapy. ACS Nano 2022, 16 (4), 6527–6540.
- (46) Li, M.; Xu, Z.; Zhang, L.; Cui, M.; Zhu, M.; Guo, Y.; Sun, R.; Han, J.; Song, E.; He, Y.; Su, Y. Targeted Noninvasive Treatment of Choroidal Neovascularization by Hybrid Cell-Membrane-Cloaked Biomimetic Nanoparticles. ACS Nano 2021, 15 (6), 9808–9819.
- (47) He, W.; Li, X.; Morsch, M.; Ismail, M.; Liu, Y.; Rehman, F. U.; Zhang, D.; Wang, Y.; Zheng, M.; Chung, R.; Zou, Y.; Shi, B. Brain-Targeted Codelivery of Bcl-2/Bcl-xl and Mcl-1 Inhibitors by Biomimetic Nanoparticles for Orthotopic Glioblastoma Therapy. *ACS Nano* **2022**, *16* (4), 6293–6308.
- (48) Liu, Y.; Lu, Y.; Ning, B.; Su, X.; Yang, B.; Dong, H.; Yin, B.; Pang, Z.; Shen, S. Intravenous Delivery of Living Listeria monocytogenes Elicits Gasdmermin-Dependent Tumor Pyroptosis and Motivates Anti-Tumor Immune Response. ACS Nano 2022, 16 (3), 4102–4115.
- (49) Dieckens, D.; Lavalaye, J.; Romijn, L.; Habraken, J. Contrastnoise-ratio (CNR) analysis and optimization of breast-specific gamma imaging (BSGI) acquisition protocols. *EJNMMI Res.* **2013**, 3 (1), 21.
- (50) Predina, J. D.; Newton, A. D.; Keating, J.; Dunbar, A.; Connolly, C.; Baldassari, M.; Mizelle, J.; Xia, L.; Deshpande, C.; Kucharczuk, J.; Low, P. S.; Singhal, S. A Phase I Clinical Trial of Targeted Intraoperative Molecular Imaging for Pulmonary Adenocarcinomas. *Annals of Thoracic Surgery* 2018, 105 (3), 901–908.
- (51) Randall, L. M.; Wenham, R. M.; Low, P. S.; Dowdy, S. C.; Tanyi, J. L. A phase II, multicenter, open-label trial of OTL38 injection for the intra-operative imaging of folate receptor-alpha positive ovarian cancer. *Gynecol Oncol* **2019**, *155* (1), 63–68.
- (52) Niikura, N.; Liu, J.; Hayashi, N.; Mittendorf, E. A.; Gong, Y.; Palla, S. L.; Tokuda, Y.; Gonzalez-Angulo, A. M.; Hortobagyi, G. N.; Ueno, N. T. Loss of human epidermal growth factor receptor 2 (HER2) expression in metastatic sites of HER2-overexpressing primary breast tumors. *J. Clin Oncol* **2012**, *30* (6), 593–9.
- (53) Blair, S.; Garcia, M.; Davis, T.; Zhu, Z.; Liang, Z.; Konopka, C.; Kauffman, K.; Colanceski, R.; Ferati, I.; Kondov, B.; Stojanoski, S.; Todorovska, M. B.; Dimitrovska, N. T.; Jakupi, N.; Miladinova, D.; Petrusevska, G.; Kondov, G.; Dobrucki, W. L.; Nie, S.; Gruev, V. Hexachromatic bioinspired camera for image-guided cancer surgery. *Sci. Transl Med.* **2021**, *13* (592), aaw7067.
- (54) Saeedi, M.; Vahidi, O.; Goodarzi, V.; Saeb, M. R.; Izadi, L.; Mozafari, M. A new prospect in magnetic nanoparticle-based cancer therapy: Taking credit from mathematical tissue-mimicking phantom brain models. *Nanomedicine: Nanotechnology, Biology and Medicine* **2017**, *13* (8), 2405–2414.
- (55) McHugh, D. J.; Zhou, F. L.; Wimpenny, I.; Poologasundarampillai, G.; Naish, J. H.; Hubbard Cristinacce, P. L.; Parker, G. J. M. A biomimetic tumor tissue phantom for validating diffusion-weighted MRI measurements. *Magn Reson Med.* **2018**, 80 (1), 147–158.

- (56) Au Pleijhuis, R.; Au Timmermans, A.; Au De Jong, J.; Au De Boer, E.; Au Ntziachristos, V.; Au Van Dam, G. Tissue-simulating Phantoms for Assessing Potential Near-infrared Fluorescence Imaging Applications in Breast Cancer Surgery. *J. Visualized Exp.* **2014**, *91*, 51776.
- (57) Liu, W.; Ruan, M.; Wang, Y.; Song, R.; Ji, X.; Xu, J.; Dai, J.; Xue, W. Light-Triggered Biomimetic Nanoerythrocyte for Tumor-Targeted Lung Metastatic Combination Therapy of Malignant Melanoma. *Small* **2018**, *14* (38), 1801754.
- (58) Wang, Y.; Ji, X.; Ruan, M.; Liu, W.; Song, R.; Dai, J.; Xue, W. Worm-Like Biomimetic Nanoerythrocyte Carrying siRNA for Melanoma Gene Therapy. *Small (Weinheim an der Bergstrasse, Germany)* 2018, 14 (47), 1803002.
- (59) Ji, X.; Ma, Y.; Liu, W.; Liu, L.; Yang, H.; Wu, J.; Zong, X.; Dai, J.; Xue, W. In Situ Cell Membrane Fusion for Engineered Tumor Cells by Worm-like Nanocell Mimics. *ACS Nano* **2020**, *14* (6), 7462–7474.
- (60) Yan, N.; Xu, J.; Liu, G.; Ma, C.; Bao, L.; Cong, Y.; Wang, Z.; Zhao, Y.; Xu, W.; Chen, C. Penetrating Macrophage-Based Nanoformulation for Periodontitis Treatment. ACS Nano 2022, 16 (11), 18253–18265.
- (61) Jia, Y.; Wang, X.; Hu, D.; Wang, P.; Liu, Q.; Zhang, X.; Jiang, J.; Liu, X.; Sheng, Z.; Liu, B.; Zheng, H. Phototheranostics: Active Targeting of Orthotopic Glioma Using Biomimetic Proteolipid Nanoparticles. *ACS Nano* **2019**, *13* (1), 386–398.
- (62) Blair, S.; Garcia, M.; Davis, T.; Colanceski, R.; Ferati, I.; Kondov, B.; Stojanovski, S.; Bogdanovska Todorovska, M.; Toleska Dimitrovska, N.; Jakupi, N.; Miladinova, D.; Petrusevska, G.; Kondov, G.; Gruev, V. An 18-band snapshot hyperspectral imaging system for sentinel lymph node dissection with multiple near-infrared fluorophores, *Molecular-Guided Surgery: Molecules, Devices, and Applications VII*, SPIE BiOS, Online, March 01, 2021; p 116250E.
- (63) Blair, S.; Garcia, M.; Zhu, Z.; Liang, Z.; Lew, B.; George, M.; Kondov, B.; Stojanoski, S.; Todorovska, M. B.; Miladinova, D.; Kondov, G.; Gruev, V. Decoupling channel count from field of view and spatial resolution in single-sensor imaging systems for fluorescence image-guided surgery. *J. Biomed. Opt.* **2022**, *27* (9), 096006.
- (64) Blair, S.; Gruev, V. Interpolant-based demosaicing routines for dual-mode visible/near-infrared imaging systems. *Opt. Express* **2022**, *30* (19), 34201–34217.